Crystallization Conditions of Basaltic Lavas Based on Clinopyroxene and Olivine Phenocrysts Petrology: A Case Study from the Neogene Lavarab Alkaline Basaltic Lavas (LABL), Eastern Iran

Sara Houshmand-Mananvi , Mehdi Rezaei-Kahkhaei , Habibollah Ghasemi , Urs Klötzli *

Posted Date: 21 April 2025

doi: 10.20944/preprints202504.0525.v2

Keywords: alkali basalt; basanite; Neogene; geothermobarometry

 doi:10.20944/preprints202504.0525.v2

Article

Crystallization Conditions of Basaltic Lavas Based on Clinopyroxene and Olivine Phenocrysts Petrology: A Case Study from the Neogene Lavarab Alkaline Basaltic Lavas (LABL), Eastern Iran

Sara Houshmand-Mananvi [1], Mehdi Rezaei-Kahkhaei [1], Habibollah Ghasemi [1] and Urs Klötzli [2,*]

[1] Department of Petrology and Economic Geology, Faculty of Earth Sciences, Shahrood University of Technology, Shahrood, Iran
[2] Department of Lithospheric Research, Faculty of Earth Sciences, Geography and Astronomy, University of Vienna, Austria
* Correspondence: urs.kloetzli@univie.ac.at

Abstract: Central aims of this project are to delineate and characterize the magma crystallization conditions associated with intra-plate volcanism after collision of the Lavarab Basaltic Lavas (LABL) in East of Iran. Their composition is more basic and includes two principal lithologies: alkali basalt and basanite, and subordinate trachy basalt. The Olivine chemistry indicates forsterite, chrysolite and hyalo-siderite compositions in the study rocks. Clinopyroxene chemistry has been used as the key component of LABL to investigate the nature of magma, tectonic setting, and physicochemical conditions of crystallization (T, P, fO_2) in basic-intermediate Lavarab lavas. The clinopyroxenes of these rocks are diopside and augite and belong to peralkaline to subalkaline magmatic series of within plate alkali basalt and volcanic arc basalt settings. Temperature and pressure estimations based on different single clinopyroxene thermobarometers indicate temperatures of ≈1110 to ≈1260 ºC, at pressures of ≈0.05 to ≈1.35 GPa corresponding to pressures equivalent to the depths of ≈2 to ≈51 km for the crystallization of clinopyroxene under the high oxygen fugacity in the lower (>30 Km) to upper (>10 Km) continental crust. Temperature estimations based on olivine-liquid thermometry are calculated temperatures of ≈1380 to ≈1390 ºC for basanites and ≈1299 to ≈1336 ºC for alkali basalts at a constant pressure of 1.4 GPa. The chemical compositions of phenocrysts in the studied basaltic lavas reflect evidence of magma recharge through multi pulses of new magma injected into the existing reservoir prior to eruptions such as petrographic evidence (absorption and rounded-shape and patchy zoned in olivine crystals and sieve texture, absorption, and oscillatory zonation in clinopyroxene crystals) and the oscillatory changes of a crystal's composition from the core to rim in the microprobe data of a crystal.

Keywords: alkali basalt; basanite; Neogene; geothermobarometry

1. Introduction

The studied lavas are located in the middle part of the Sistan Suture Zone, east of Iran. The prior studies of this zone are related to the characteristics, origin and tectonic setting of igneous rocks by [1]. Tirrul et al. [2] also provided an interpretation of the tectonics of the Sistan Suture Zone in east of Iran. Tirrul et al. [2] attribute the beginning of convergence and obduction of ophiolites to Late Cretaceous. They believe that the result of this collision was the creation of the Ratuk (Upper Cretaceous) and Neh (Senonian to Eocene) ophiolitic complexes as accretionary prisms and the Sefidabeh basin as a fore-arc basin. In addition, the magmatic events in eastern Iran have produced subvolcanic and intrusive bodies, as well as lava flows, pyroclastics, and volcanic-clastic derivatives which interlayered with the detrital and carbonate deposits of this basin (e.g., [1,3–7]).

 doi:10.20944/preprints202504.0525.v2

The lava flows are located in the southern part of Sefidabeh Basin. These lavas have originally been interpreted as basalts being Oligocene-Miocene in age ([8–10]).

On one hand, the composition of the Lavarab Basaltic Lavas (LABL) is more basic as a direct product of mantle melting. This leads to understand the characteristics of the upper mantle beneath the LABL and petrological developments related to Sistan Suture Zone. On the other hand, phenocrysts in basalts indicate that they underwent a period of crystallization in a semi-deep magma chamber(s) during the ascent of magma from the mantle to the surface [11]. Therefore, by understanding the minerals that formed in the magma chamber before eruption, it is possible to understand magma chamber processes [11]. Currently, the chemical nature of the crystallization conditions of minerals, the formation and evolution of the magma that forms igneous rocks, and to determine the tectonic environment (e.g., [12,13]) in which it was formed, mineral chemistry is crucial. Mineral chemistry reflects the chemistry of the crystallizing magma, and resistant minerals against alteration and weathering, such as clinopyroxene, play a more significant role compared to other minerals. Pyroxene and olivine, as the main mineral components of the Oligocene-Miocene LABL rocks, reflect the composition of the parental magma, the physicochemical conditions prevailing during crystallization in the magma chamber(s), and the tectonic environment of the parental magma formation. Olivine and pyroxene frequently crystallize early in magmatic systems, as is the case in the Lavarab basaltic lavas. Previously, the composition of clinopyroxene (as a resistant mineral against alteration and weathering) has been used to estimate the temperature, pressure, and oxygen fugacity during the crystallization of the magma that formed it, and various thermobarometer formulations have been proposed for this purpose [13–24]. Xu [25] expressed that estimates of the crystallization temperatures of Mg-rich magmas are critical for understanding the thermal state of the mantle and testing the mantle plume model [1,26–28]. The olivine-melt equilibrium-based thermometer was conventionally thought to be one of the most precise methods available [29–31]. However, olivine thermometry requires determination of a primary magma composition that is equilibrated with olivine in the mantle source (or maximum forsterite content of olivine phenocrysts observed). These parameters may lead to ambiguous results [32] if using the same data with slightly different assumptions to calculate the primary melt compositions (e.g., [31,33]).

The purpose of the present study is to clarify the LABL magma crystallization condition based on the composition of mafic minerals on the focus of mineral-liquid equilibrium and single mineral methods. In this paper, the mineral chemistry of clinopyroxene and olivine phenocrysts separately investigate for all rock types (basanite, alkali basalt, and trachy basalt) in order to know the conditions of the first stage of crystallization. So far, no data has been published regarding the mineral chemistry of the LABL.

2. Geological Setting and Study Area

Iran is located in the middle part of the Alpine-Himalaya folded belt. This belt is the site of the collision between the two supercontinents, Eurasia and Gondwana, beginning from western Europe and continuing through Turkey, Iran, Afghanistan, to Tibet, near Burma and Indonesia ([34,35]). In this belt intra-continental collision zones exhibit complex geometries and a high diversity in scale and strain history [36]. The development of the mountain ranges of eastern Iran (the Sistan Suture Zone) is a simple example, as in this area subduction did not lead to the creation of a widespread magmatic arc, because the destruction of a narrow strip of oceanic lithosphere occurred in a short period of time [2]. The Ratuk and Neh ophiolitic complexes as accretionary prisms and the Sefidabeh basin as a forearc basin were the results of this collision.

The studied lavas are located in the Sefidabeh basin in a nearly north-south trend. The age of the deep to shallow marine deposits of Sefidabeh is Maastrichtian-Paleogene and includes interlayers of lavas, pyroclastics, and volcaniclastic derivatives with detrital and carbonate rocks [1], deposited in a forearc basin. Its eastern border with the Afghan block is formed by the Harirud fault and its lower border with the basement is described to be the Talkhab thrust fault [37]. After the eruption of basaltic lavas in the region, the sedimentary environment gradually deepened, and horizons of marl were

 doi:10.20944/preprints202504.0525.v2

deposited alternating with clastic rocks [9]. The occurrence of the Sistani event [38], equivalent to Pyrenean orogeny in east Iran, caused the folding of Cretaceous-Paleogene rocks during the Oligocene and continued until the Neogene [9]. The morphology of the lavas and the type of their detrital hosted rocks indicate that these lavas erupted in a continental alluvial-fluvial or lacustrine environment. Eocene flysch is located further south and west of the region and is composed mostly of fine-grained sandstones and shale, and host numerous granitoid bodies ([1,2,39–41]). The LABL are related to the post-continental collision with a within-plate tectonic setting. These lavas were formed from the low degree partial melting of the upwelled asthenosphere due to the delamination of thickened lithosphere root [42]. With the ascent of the asthenosphere and the thinning of the lithosphere due to delamination, a tensional regime has occurred in the region, and the activity of the Zahedan and Hariroud transtensional faults have created a suitable path for ascending melts [42].

3. Field Relationship and Petrography

The location and geological map of Lavarab area are illustrated in Figure 1. These rocks form elongated outcrops (up to 20 km) and have a maximum width of approximately 2 km in a north-south trend (N338) parallel to and close to the Zahedan dextral fault in the west. In the study area, there is an asymmetric syncline with a north-south axis, in which the lavas are visible on its west and east limbs. The lavas are concordant with the Oligocene-Miocene sediments. Two eruption stages are observed on the eastern limb of syncline. After the first one, a 20-meter-thick sedimentary sequence was deposited on it, and then the second eruption occurred. It seems that the first eruption is thicker and more extensive than the second one, so that its continuation can also be seen on the western limb. It seems some parts of basaltic magma erupted phreatically and some of them exploded on the surface that created columnar structures. In the phreatic eruptions there are no pillow structures, but oxidation and alteration cause colorful appearance of the lavas, so they must be erupted in a shallow depth (up to 30 m) what is confirmed by Ostracoda (*Cytherella* sp. and *Cytheridea* sp.) in marl which is located under the study lavas (at the intersection of the road with the lava in the southern part of the outcrop (see Figure 1). Other paleontological findings of these marls include benthic foraminifera such as *Pararotalia* sp., *Elphidium* sp., *Osangularia* sp., and *Asterigerina* sp., all of which together indicate that these marls belong to the Early Miocene. An annular outcrop of the lavas is observed in the southeast of LABL which probably erupted at the intersection of a NW-SE dextral fault with a NE-SW sinistral fault in a local tensile environment. Some field observations related to LABL are presented in Figure 2. These melanocratic to mesocratic lavas are porphyritic (relatively micro/phenocryst-rich, up to ~%45), and classified in three main groups based on petrography as follow:

 doi:10.20944/preprints202504.0525.v2

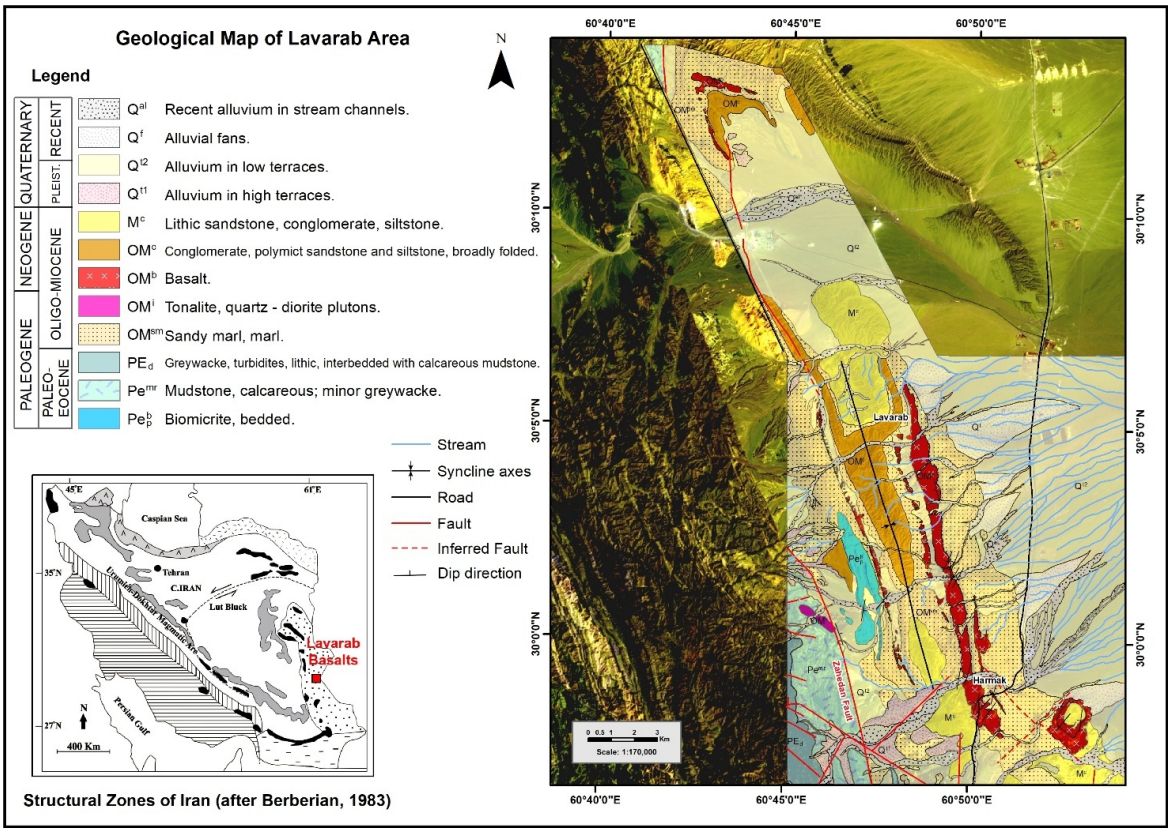

Figure 1. Geological map of the Lavarab basaltic rocks which prepared by using of the detailed field sur-vey-ing of this research and basic information of the regarding geological maps ([8,10] in scale of 1:250000 and [9] in sclae of 1:100000). Structural Zones of Iran is modified by Rezaei-Kahkhaei et al. [43].

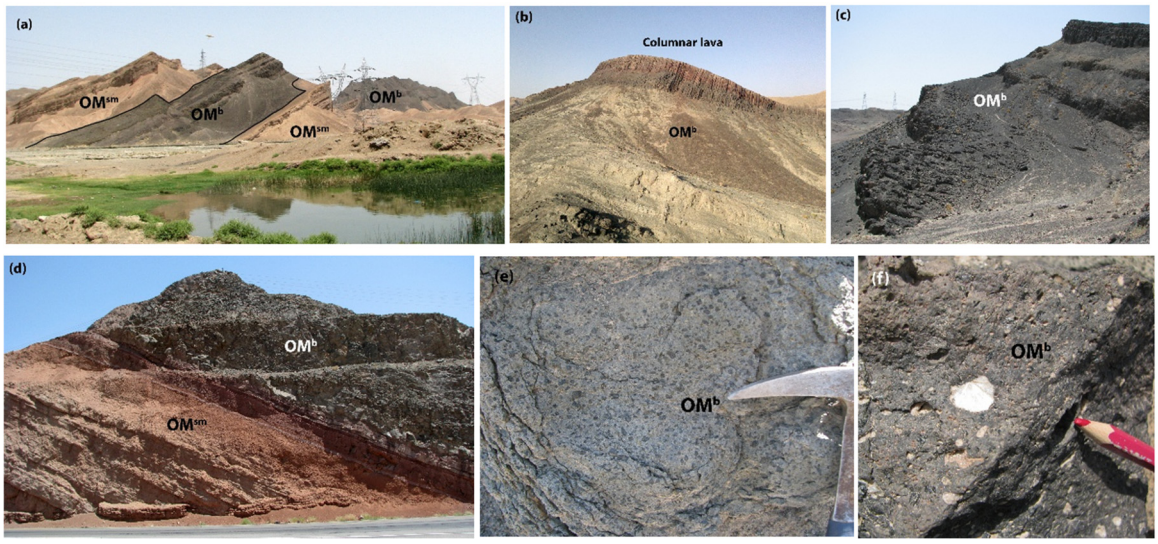

Figure 2. (a) A view of the Oligocene-Miocene sediments (OM^{sm}) and interlayering of basalt (OM^{b}) with a slope to the west, around the Harmak village, view to the northwest; (b) a view of massive lavas at the bottom and columnar lavas at the top; (c) a view of Lavarab lava flow, view to the southwest; (d) Backed Oligocene-Miocene sandy marl (OM^{sm}) sediments below the Oligocene-Miocene lavas (OM^{b}), Entrance of Harmak village, view to the east; (e) onion skin weathering and pyroxene phenocrysts in in the Lavarab lavas; (f) Vesicles in different sizes filled with zeolite.

3.1. Trachy Basalt

The lavas are porphyritic or vesicular in texture with a microlithic to aphanitic matrix. The rocks contain 30% micro/phenocrysts (<~3000 μm in length, ~20% plagioclase, ~10% clinopyroxene). The tabular plagioclase and

 doi:10.20944/preprints202504.0525.v2

euhedral to subhedral pyroxene micro-phenocrysts (100-500 μm) and phenocrysts are existing. The polysynthetic twins, zonation and sieve texture is common in the plagioclases. Simple and lamellar twins and 8-side sections are observed in clinopyroxene (mostly augite). Few opacity minerals are observed, that are similar to amphibole. The cavities are mostly filled by calcite. The accessory minerals consist of apatite and opaque minerals. A photomicrograph of trachy basalt is shown in Figure 3a.

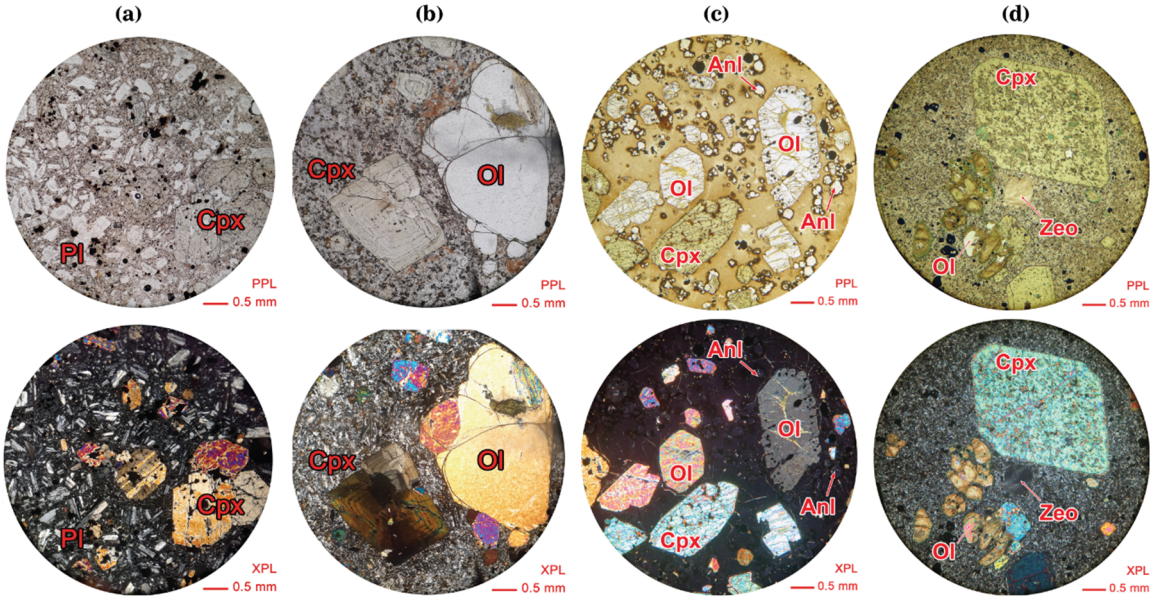

Figure 3. Photomicrographs (in parallel-polarized and cross-polarized lights). (a) Plagioclase and clinopyroxene micro-phenocrysts/phenocrysts in trachy basalt; (b) Oscillatory zoning and hourglass twinning of clinopyroxene in alkali basalt; (c) Olivine and clinopyroxene phenocrysts and analcime micro-phenocrysts within a glassy matrix in alkali basalt; (d) Clinopyroxene euhedral phenocryst with sieve texture, altered olivine, and a cavity is filled by zeolite in basanite. Abbreviations are: Cpx: clinopyroxene, Pl: plagioclase, Ol: olivine, Anl: analcime, Zeo: zeolite.

3.2. Alkali Basalt

The alkali basalts are porphyritic or vesicular in texture with a microlithic or glassy matrix. The cavities are mostly filled by zeolite. These lavas contain 35-45% micro/phenocrysts (<1 cm in length) comprising ~ 20-30% clinopyroxene, ~ 5-10% olivine, ~ 5% analcime, and rare Fe–Ti oxides. The euhedral to subhedral pyroxene, subhedral to euhedral olivine, and euhedral analcime are visible as micro-phenocrysts and phenocrysts. The maximum size of pyroxene is up to 1 cm as mega-phenocrysts in alkali basalts. Clinopyroxene crystals are typically euhedral and indicating two pyroxene generations: one with sieve texture and another without it. Clear oscillatory zoning and hourglass twinning of clinopyroxene phenocrysts are observed in alkali basalt (Figure 3b). Analcime is also seen as rounded micro-crysts and euhedral micro-phenocrysts scattered in the glassy matrix, and embayed crystals and skeletal growth are observed in olivines (Figure 3c). Apatite inclusions are abundant in pyroxene but also form fine needles in the matrix. Opaque minerals are also found in fine-grained, cubic, and sometimes dendritic habit in abundance in the grounmass or as inclusions within phenocrysts, especially olivines. A photomicrograph of alkali basalt is shown in Figure 3b,c.

3.3. Basanite

This group of lavas is porphyritic or vesicular in texture with a fine-grain to microlithic, and rarely glassy matrix. The lavas contain 35-40% phenocrysts comprising ~20-30% clinopyroxene, 10-15% olivine, ~5% analcime. Rare Fe-Ti oxides also occur. In some rocks, olivine crystals are mostly disintegrated to chlorite and iddingsite (Figure 3d). Clinopyroxene micro-phenocrysts and phenocrysts are mostly euhedral. An ultramafic sample (L.57) contains 15% phenocrysts (<~1500 μm in

 doi:10.20944/preprints202504.0525.v2

length) comprising ~14% olivine, and rare clinopyroxene. A photomicrograph of trachy basalt is shown in Figure 3d.

The groundmass in both alkali basalts and basanite comprises of microphenocrysts (<10 to ~100 mm in size) of the same phases and in the same relative abundances as found in the phenocryst population. Plagioclase microliths are commonly euhedral to subhedral, while the other phases are anhedral. Sanidine also occur in fine-grain (~0.25 mm) groundmass.

4. Analytical Technique

4.1. Whole Rock

Based on geological mapping and satellite imagery 120 samples from all (?) different rock units were collected. Among them, 70 thin sections of Lavarab Basic Lavas were examined using optical microscopy to characterize their mineralogy. Then 18 fresh samples with minimal alteration and proper spatial distribution in the area were selected for whole rock geochemical analyses. The chemical analyses of the main elements have been made by XRF method at the laboratory of Geological Survey of Iran (GSI), whereas the trace and rare earth elements were determined by ICP-MS and ICP-OES at the laboratory of Applied Research Center of GSI in Alborz, Iran). The loss on ignition was determined by weight difference after ignition at 1000 °C by the wet chemistry method in the laboratory of the GSI. The detection limit is 0.1 wt% for major oxides, from 0.1 to 1 weight-ppm for trace elements and from 0.1 to 0.5 weight-ppm for the rare earth elements.

4.2. Electron Probe Micro-Analyzer (EPMA)

Seven samples were prepared for electron microprobe analyses, including one trachy basalt (L.10), four alkali basalt (L. 38, L.51, L.61 and L.81), and two basanites (L.57 and L.65). Backscatter electron (BSE) imaging of clinopyroxene and olivine in polished thin sections were used to investigate zonation patterns of crystal populations, and select crystals for geochemical analysis. Quantitative spot analyses were performed on a CAMECA SX 100 electron microprobe at Micro-Area Analysis Laboratory, Polish Geological Institute (Warsaw, Poland), using a 15 kV acceleration voltage, 20 nA current, a spot size of 5 μm and 10s counting time on peak position.

4.3. Test for Equilibrium in Mineral-Liquid Geothermobarometry

MagMin_PT program [44] calculates $KD(Fe–Mg)^{ol–liq}$ using equations 1 and 2 (originally suggested for olivine by Roeder and Emslie (1970)) to test for equilibrium between olivine and liquid and between clinopyroxene and liquid.

$$MgO^{min} + FeO^{liq} = MgO^{liq} + FeO^{min} \quad (1)$$

$$KD(Fe\text{-}Mg)^{min\text{-}liq} = XFe^{min}XMg^{liq} / XMg^{min}XFe^{liq} \quad (2)$$

4.4. Programs to Calculate Temperature and Pressure

MagMin_PT is using to determine temperature based on glass or whole rock composition as well as olivine thermometry. For clinopyroxene, Seosoo [21] thermo-barometers were calculated in Excel software, the thermo-barometer calculations of Nimis [45], Nimis and Tylor [22], Putirka et al. [46,47], Putirka [23] were made using WinPyrox [48], and Nimis and Ulmer [22] and Neave and Putirka [49] thermo-barometers were calculated by using MagMin_PT [44] program.

 doi:10.20944/preprints202504.0525.v2

5. Results

5.1. Whole Rock Composition

The geochemical characteristics of the whole rock of LABL indicate the dominant alkaline sodic nature ([Na_2O + K_2O] = 4.13–8.11 wt% and K_2O/Na_2O = 0.13–1.62) (Table 1). The lava compositions are more basic and include alkali basalt, basanite, and less trachy andesite based on the nomenclature of Winchester and Floyd [50] (Figure 4). The LABL has the characteristics of low to middle SiO_2 contents (43.76–53.91 wt%), high alkali contents (4-8 wt%), and high CaO contents (7.39–10.83 wt%). MgO contents range from 3.01 to 13.38 wt %, and the Mg# (Mg#=100 $Mg^{2+}/[Mg^{2+}+Fe^{2+}]$) ranges from 53.60 to 83.24 (mean = 74.51). Al_2O_3 contents vary from 12.97 to 17.88 wt%. The TiO_2 contents ranges from 0.47-1.79 wt% (mean = 0.8 wt%), so these rocks are low-Ti type [51,52]. These results show a close affinity with intraplate alkaline basalts and continental rift alkaline basalts [53]. The compatible trace element Ni shows clear correlations with MgO contents, as well as the trend between Cr and MgO. The concentrations of Cr and Ni are 59.6-690.3 ppm and 31.4–537.3 ppm, respectively. To find more detail information about the whole rock geochemistry of LABL refer to [42].

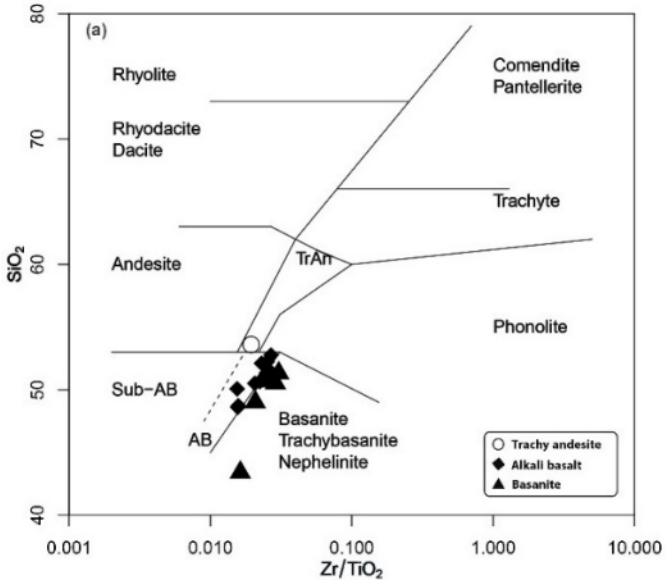

Figure 4. SiO_2 vs. Zr/TiO_2 diagram for classification of the studied rocks [50].

Table 1. Whole rock chemical analysis of Lavarab basic lavas. The names of the rocks are determined based on the classification of Winchester and Floyd (1977) and are as follows: TA: trachy andesite; AB: alkali basalt; Bs: basanite.

Sample No.	L.10	L.37	L.51	L.52	L.61	L.75	L.81	L.86	L.87	L.92	L.100	L.13	L.44	L.42	L.53	L.64	L.80	L.57
Long (UTM)	295332	873628	786288	842920	528861	290812	909129	117291	982895	829570	290222	893028	884290	062908	127983			
	7	9	7	2	9	8	2	2	6	8	9	1	8	5	2	5	2	0
Lat (UTM)	331623	322633	292333	296331	863318	733190	331923	319133	176332	673317	033235	332353	332963	232393	319033	427		
	72	75	20	09	18	62	96	86	36	70	02	73	39	32	09	67	96	86
Rock type	TA	AB	AB	AB	AB	AB	AB	AB	AB	AB	AB	Bs	Bs	Bs	Bs	Bs	Bs	Bs
SiO_2	52.7	49.65	47.37	48.58	46.93	49.6	49.33	51.27	48.72	48.9	49.9	49.2	49	47.92	48.72	49.14	49.66	42.37
TiO_2	0.85	0.79	0.64	0.75	1.71	0.77	0.78	0.72	0.83	0.69	0.73	0.69	0.68	0.45	0.63	0.78	0.7	1.67
Al_2O_3	17.48	13.52	15.46	12.53	15.91	13.23	13.13	13.64	15.22	15.71	13.17	14	13.01	13.66	12.41	12.81	13.4	14.42
Fe_2O_3T	8.31	8.33	9.09	9.21	9.12	8.63	8.57	7.73	8.87	8.29	8.19	8.61	7.59	9.33	337.59	9.35	8.19	11.66
MnO	0.13	0.15	0.19	0.19	0.11	0.13	0.16	0.15	0.15	0.16	0.13	0.18	0.16	0.18	0.14	0.13	0.16	0.19
MgO	2.94	7.72	9.69	8.15	8.32	7.55	6.81	7.7	8.45	6.69	7.91	8.87	10.16	13	11.45	7.87	8.3	11.12
CaO	9.49	8.32	9.61	9.92	8.38	8.4	9.04	7.15	9.55	8.97	8.11	7.95	8.32	8.94	7.35	8.85	8.13	10.48

 doi:10.20944/preprints202504.0525.v2

Sample No.	L.10	L.37	L.51	L.52	L.61	L.75	L.81	L.86	L.87	L.92	L.100	L.13	L.44	L.42	L.53	L.64	L.80	L.57
Na_2O	3	3.88	3.05	4.53	3.56	4.1	4.04	4.12	1.9	4.25	4.83	3.39	3.46	2.3	3.31	4.26	3.87	4.47
K_2O	2.77	3.1	1.97	1.24	1.48	1.68	3.38	3.73	3.08	2.58	1.9	3.24	3.64	1.71	3.49	2.35	3.41	0.59
P_2O_5	0.6	0.85	0.37	0.8	0.8	0.87	0.89	0.98	0.54	0.57	0.88	0.75	0.95	0.27	1.01	0.89	0.93	0.63
LOI	1.35	3.09	1.98	3.4	3.35	4.46	3.36	2.32	2.42	2.85	3.63	2.65	2.39	1.7	3.26	2.92	2.56	2.08
Mg#	53.6	75.55	76.6	73.74	73.66	73.67	72.87	77.63	74.66	72.69	76.18	77.19	81.69	80.59	83.24	73.42	77.36	73.96
A/NK	3.03	1.94	3.08	2.17	3.16	2.29	1.77	1.74	3.06	2.3	1.96	2.11	1.83	3.4	1.82	1.94	1.84	2.85
A/CNK	1.15	0.88	1.06	0.8	1.19	0.93	0.8	0.91	1.05	0.99	0.89	0.96	0.84	1.05	0.88	0.83	0.87	0.93
K_2O+Na_2O	5.77	6.97	5.03	5.77	5.04	5.78	7.42	7.84	4.97	6.83	6.73	6.63	7.11	4.01	6.8	6.61	7.28	5.06
K_2O/Na_2O	0.92	0.8	0.65	0.27	0.42	0.41	0.84	0.91	1.62	0.61	0.39	0.96	1.05	0.75	1.06	0.55	0.88	0.13
Cs	0.65	7.67	0.95	7.26	0.97	7.54	4.77	4.68	1.74	11.98	9.07	3.66	3.52	0.65	6.13	6.35	3.79	1.19
Ba	991	1387	442	902	748	1271	1123	1542	957	989	1160	1235	1547	409	1462	1259	1475	822
Rb	75	173	66	108	40	168	216	79	64	51	158	77	100	27	75	145	125	24
Sr	800	1010	1130	1121	913	819	840	789	507	674	811	812	843	518	718	952	954	698
Pb	11.69	19.49	5.38	15.28	2.71	17.61	17.4	18.44	9.57	10.98	16.81	16.41	17.32	6.61	17.73	18.37	17.91	5.08
Th	5	9.34	2.64	7.41	4.24	9.83	9.62	10.59	4.03	4.57	8.25	7.67	8.53	2.21	8.89	8.68	10.87	8.3
U	1.4	2.77	0.71	2.22	0.91	3.23	3.16	2.43	1.09	1.41	2.47	2.15	2.39	0.64	2.66	2.63	2.88	1.64
Zr	167	213	103	174	280	204	203	200	131	147	175	185	203	97	178	200	221	278
Ta	2.37	1.21	0.46	1.05	3.6	1.39	1.19	1.05	0.93	1.32	0.92	0.84	0.93	0.5	1	1.19	2.16	3.63
Hf	5.77	6.23	3.38	5.38	7.83	5.88	5.84	5.36	3.95	4.33	5	5.53	5.88	3.03	5.55	6.01	6.39	7.55
Y	26.4	23.93	16.55	22.56	20.38	22.08	22.14	21.2	21.66	23.06	20.75	22.37	24.24	14.87	21.5	23.24	23.62	24.68
Nb	23.4	18.5	14.2	15.3	38.9	19.8	18.1	20.6	17.9	19.7	18.2	19	20.6	12.6	18.7	17.9	20.2	47
La	20.74	30.2	14.19	25.22	32.18	28.61	26.91	27.1	15.98	17.54	25.62	25.87	28.35	13.06	28.3	27.28	29.54	51.61
Ce	35.28	49.82	23.97	43.12	53.87	46.69	44.23	45.33	27.06	29.34	43.24	42.22	47.74	22.16	46.61	45.56	49.12	83.62
Pr	5.16	7.07	3.64	6.15	8.18	6.72	6.23	6.18	3.95	4.38	6.19	5.92	7.04	3.19	6.39	6.5	7	11.28
Nd	20.05	27.56	13.66	25.28	31.18	25.02	24.07	24.19	16.3	17.92	23.94	22.8	26.23	11.92	24.67	25.95	25.99	40.94
Sm	6.1	7.29	3.27	6.27	7.1	6.44	6.69	6.58	4.76	5.27	6.58	6.32	6.93	2.95	6.89	7.07	7.12	7.17
Eu	2.21	2.61	1.01	1.92	2.48	2.24	2.23	2.12	1.5	1.8	2.01	2.22	2.45	0.98	2.55	2.42	2.5	2.15
Gd	3.88	4.65	2.49	4.32	4.96	4.41	4.45	4.37	3.07	3.67	4.07	4.11	4.67	2.35	4.42	4.64	4.46	5.83
Tb	0.74	0.76	0.48	0.81	0.88	0.71	0.75	0.74	0.64	0.69	0.76	0.7	0.72	0.4	0.78	0.78	0.71	0.99
Dy	4.01	4.23	2.66	4.11	3.94	3.6	3.68	3.56	3.4	3.89	3.82	3.53	4.19	2.28	3.92	4.19	3.76	5.5
Ho	0.99	0.86	0.59	0.8	0.81	0.79	0.8	0.68	0.8	0.84	0.75	0.83	0.87	0.54	0.74	0.9	0.82	0.9
Er	2.63	2.47	1.61	2.16	2	2.29	2.04	2.04	2.11	2.44	2.05	2.18	2.43	1.46	2.09	2.27	2.42	2.4
Tm	0.48	0.42	0.31	0.36	0.3	0.4	0.36	0.37	0.34	0.42	0.38	0.39	0.4	0.25	0.38	0.38	0.41	0.4
Yb	2.86	2.43	1.4	1.83	1.62	2.32	2.2	1.71	1.73	2.17	1.84	2.37	2.44	1.49	1.82	2.4	2.4	1.61
Lu	0.55	0.46	0.28	0.39	0.3	0.38	0.4	0.4	0.38	0.44	0.36	0.4	0.48	0.28	0.36	0.46	0.47	0.36
Ga	19.54	12.91	11.82	9.99	18.65	12.62	12.33	12.18	12.37	13.56	11.03	13.3	12.43	10.33	12.08	12.22	12.72	15.13
Sc	34.03	34.78	35.67	35.49	20.7	28.79	32.93	27.18	32.46	36.25	29.66	33.96	37.52	29.21	31.17	34.34	32.05	27.29
V	327.09	217.86	204.78	184.8	193.05	224.91	207.33	227.39	240.89	265.85	214.23	240.73	227.47	176.06	220.26	213.96	226.78	234.31
Cr	59.6	524.2	428.5	526.8	256.8	417.5	384.8	372.9	321	378.9	690.3	450.7	736	632.2	542.7	671.5	346.4	432.3
Co	28.29	39.2	44.97	35.07	34.86	32.64	31.49	30.81	30.71	34.43	33.04	37.19	34.96	53.29	32.55	38.92	32.45	45.91
Ni	31.41	190.59	356.86	186.95	114.44	130.53	122.14	130.2	78.56	77.23	188.87	190	200.64	537.26	185.03	208.87	127.5	267.22
Cu	77.53	126.4	65.22	91.69	62.15	134.93	115.26	130.57	66.68	112.75	107.08	114.46	119.87	71.42	122.49	105.72	115.45	77.98
Zn	91.43	71.29	64.71	68.79	91.25	68.4	64.58	68.27	70.21	74.31	69.02	73.24	70.78	63.38	66.69	70.72	70.6	85.38
Ti	6490.43	5274.53	4809.65	4688.33	12425.2	4728.06	4965.11	4929.6	4929.6	5581.54	4700.39	5362.5	5390.8	3542.09	4700.39	4935.31	4972.23	10551.2
Mn	1138.84	1201.86	1100.56	1102.14	1026.95	1095.78	1056.61	1001.35	1014.64	1083.29	1015.75	1143.2	1090.14	1064.18	995.81	1132.2	1035.97	1212.9
W	0.86	1.8	0.18	1.66	0.11	1.81	1.79	<0.10	<0.10	<0.10	1.86	0.55	0.76	<0.10	0.34	1.79	1.47	0.47

 doi:10.20944/preprints202504.0525.v2

5.2. Mineral Chemistry

In this regard more than 950 points on 272 crystals were analyzed from pyroxene and olivine on mega-phenocrysts (0.5-1 cm), phenocrysts 0.5-5 mm), micro-phenocrysts (0.1-0.5 mm) and micro-crysts (<0.1 mm) of olivine and clinopyroxene in 7 samples of LABL (see Supplementary data).

5.2.1. Olivine

Olivine is only present in basanites and alkali basalts. Olivine ranges from Fo_{70} Fa_{29} $Tp_{0.8}$ to Fo_{94} Fa_{6} $Tp_{0.05}$ show forsterite and chrysolite composition in basanite (data from 24 crystal, n = 97), and from Fo_{72} Fa_{27} $Tp_{0.08}$ to Fo_{92} Fa_{7} Tp_{1} in alkali basalt indicate forsterite, chrysolite and hyalosiderite composition (data from 55 crystal, n = 187) (Figure 5). Olivine phenocrysts in the basanite are normally zoned with broad core regions ($Fo_{86–91}$) and outer rim zones that grade to lower Mg contents ($Fo_{71–76}$) (Figure 6a).

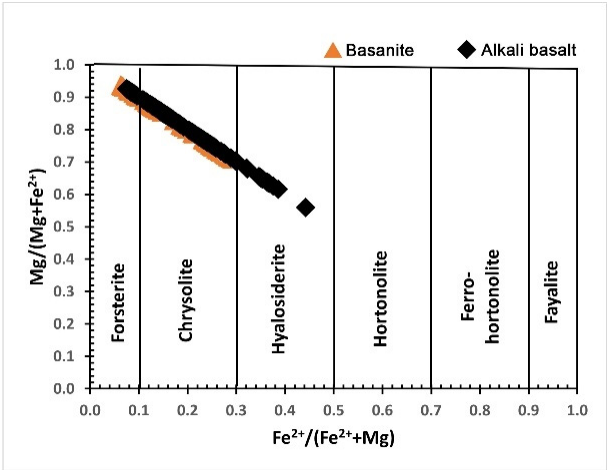

Figure 5. Determination of the olivine types in Lavarab lavas.

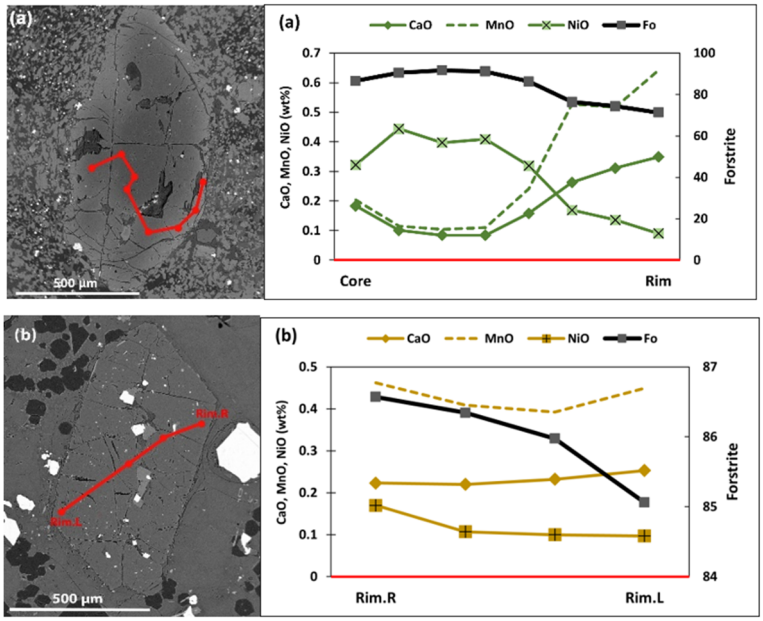

Figure 6. Examples of BSE images and compositional traverses of olivine crystals from (a) Patchy-zoned and resorbed wide core crystal with low-Fo and Ni, but high-Mn rim overgrowth (basanite, L.57); (b) Generally, a euhedral homogenic crystal (alkali basalt, L.38). Red line and points on image show location of geochemical traverse from core to rim and analyzed points, respectively.

 doi:10.20944/preprints202504.0525.v2

Rim-ward minor element trends include depletion in Ni, enrichment in Mn, and weak enrichment in Ca. Olivine phenocrysts in alkali basalt display similar textural and compositional characteristics (Figure 6b). Their core regions are characterized by ~Fo_{86} contents and the rims are invariant with $Fo_{85\text{-}86.5}$. Micro-phenocrysts in both rock groups (100-500 μm) are anhedral, non-zoned and have invariance Mg contents (~$Fo_{70.4\text{-}87}$).

5.2.2. Clinopyroxene

Pyroxenes are Ca-Mg-Fe rich [54] and classified as diopside and augite [55] in all rock types (Figure 7a,b). Examples of BSE images and compositional traverses of LABL clinopyroxene crystals of each rock type are shown in Figure 8. Patchy-zoning and oscillatory zonation occur in some crystals. In order to compare the exact pyroxene compositions and understand the magma evolutions during ascent and cooling based on the crystal size and its composition, one sample from each rock are selected (L.81 with SiO_2=49.3 wt% from alkali basalts, L.57 with SiO_2= 42.3 wt% from basanite, and L.10 with SiO_2=52.7 wt% from trachy basalt). According to the crystal size, the clinopyroxene mineral chemistry data of mention samples are divided in three groups including micro-phenocrysts (0.03-0.5 mm or 30-500 μm), phenocrysts (0.5-5 mm), and mega-phenocrysts (5-1000 mm) as follow:

- **Cpx Mega-phenocrysts**

This group of crystals (0.5 and 1 cm in length) are found in alkali basalt (L.81), but are absent in basanite and trachy basalt. According to binary plot (data from 4 crystals, n = 38), all data are located in the range of Ca-Mg-Fe rich with more diopside composition which show compositional range from $Wo_{44}En_{42}Fs_8$ to $Wo_{46}En_{47}Fs_{12}$.

- **Cpx Phenocrysts**

The clinopyroxene phenocrysts (0.5-5 mm in length) are found in alkali basalt (L.81) and trachy basalt (L.10) whereas being absent in basanite (L.57). According to the binary plot (Q-J), all Cpx pyroxene phenocrysts are located in the range of Ca-Mg-Fe rich Cpx in both the alkali basalt and trachy basalt. The alkali basalt Cpx is diopside and augite ($Wo_{42}En_{42}Fs_5$ to $Wo_{46}En_{51}Fs_{12}$) as well as trachy basalt ($Wo_{40}En_{42}Fs_8$ to $Wo_{47}En_{47}Fs_{15}$) with a higher abundance of augite (data from 5 crystals, n = 51 for alkali basalt, and 7 crystals, n = 57 for trachy basalt). Patchy-zoning or oscillatory-zoning are observed in the clinopyroxenes.

- **Cpx Micro-phenocrysts**

The third group of crystals (0.1-0.5 mm in length) are observed in trachy basalt (L.10) and basanite (L.57), whereas being absent in alkali basalt (L.81). Pyroxene micro-phenocrysts in basanite are Ca-Mg-Fe rich and contain Ca and Mg pyroxene with diopside ($Wo_{47}En_{33}Fs_8$ to $Wo_{52}En_{45}Fs_{15}$; data from 9 crystals, n = 22). According to the classification of Morimoto et al. [55], pyroxene micro-phenocrysts are augite and diopside. Pyroxene micro-phenocrysts in trachy basalt are characterized by Ca, Mg-rich pyroxenes with a higher abundance of augite and lower abundance of diopside components ($Wo_{40}En_{40}Fs_{11}$ to $Wo_{46}En_{47}Fs_{15}$).

The modeling of the compositional differences of the mentioned crystals is shown in Figure 9 for better comparison.

 doi:10.20944/preprints202504.0525.v2

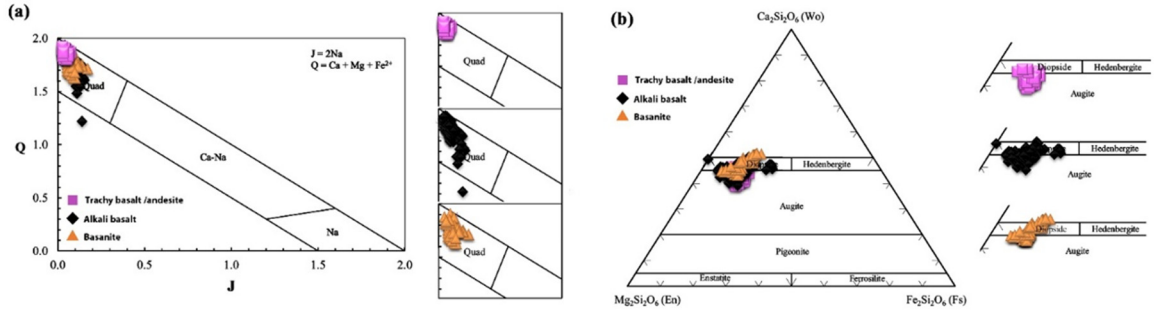

Figure 7. (a) Q-J Diagram [54]; (b) Pyroxene Classification [55] for all clinopyroxenes related to Lavarab lavas. Data from 206 crystal, n = 776.

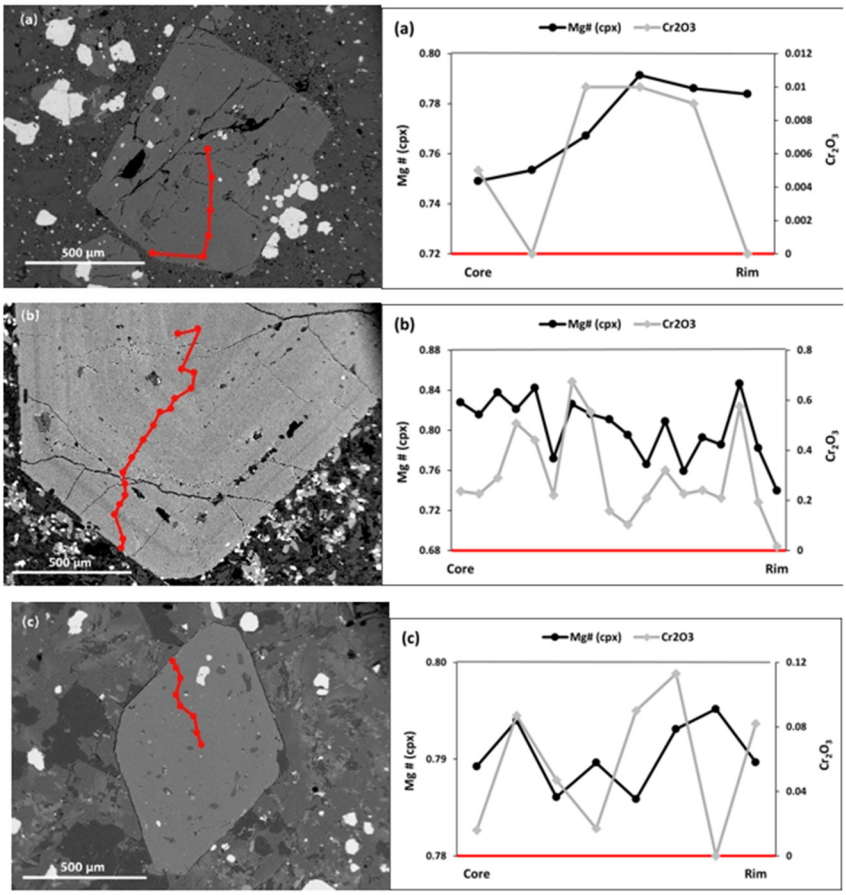

Figure 8. Examples compositional traverses of LABL clinopyroxene crystals. (a) Low-Mg and Cr reversed zoned clinopyroxene with a high-Mg and Cr rim (trachy basalt, L.10); (b) Oscillatory, generally normal zoned crystal lacking a prominent resorbed core with fluctuations in Mg and Cr values from core to rim as a sign of different pulse injections in magma chamber(s) (Alkali basalt, L.51); (c) Typical euhedral crystal with fluctuations in Mg and Cr values from core to rim lacking resorbed core (basanite, L.65). Red line and points on image show location of geochemical traverse from core to rim and analyzed points respectively.

 doi:10.20944/preprints202504.0525.v2

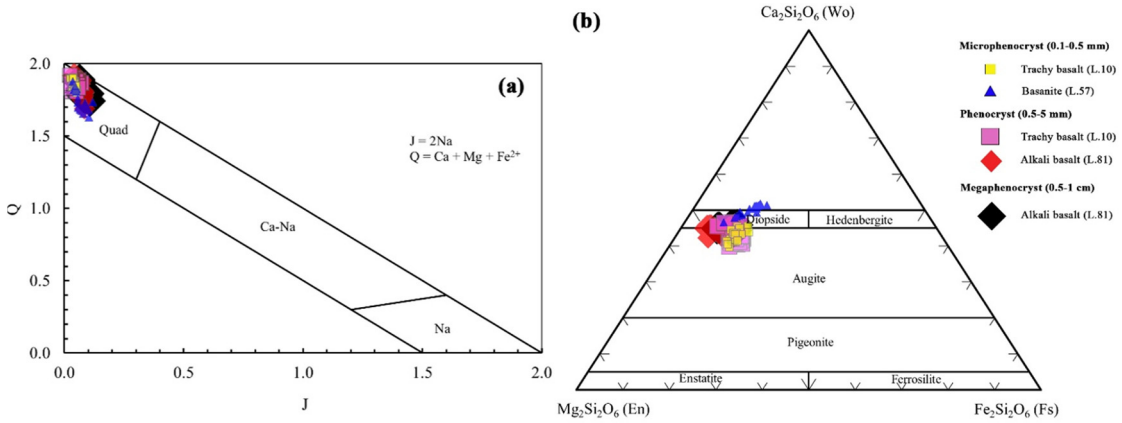

Figure 9. (a) Q-J Diagram [54]; (b) Pyroxene Classification [55] for clinopyroxene micro-phenocrysts, phenocrysts and mega-phenocrysts in trachy basalt (L.10), alkali basalt (L.81) and basanite (L.57) of the Lavarab lavas.

6. Discussion

6.1. Crystallization Conditions

Due to the impossibility of directly measuring intensive parameters (temperature, pressure, and oxygen fugacity) during magma generation, movement and accumulation in magma chambers, as well as its crystallization and emplacement within the crust, geoscientists commonly use indirect methods to understand these conditions. One such method involves utilizing the equilibrium composition between coexisting minerals and the melt from which they were crystallizing. Determining these conditions is based on the thermodynamic principles of mineral-melt equilibrium, achieved by characterizing the chemical properties of experimental products analogous to the compositions of igneous minerals and their coexisting melts [24,56]. Olivine compositions are widely used to constrain magmatic thermodynamic conditions such as magmatic temperature, oxygen fugacity, and H_2O content. However, elemental diffusion may change the initial compositions and lead to large uncertainty on the estimation of these thermodynamic conditions [28]. Arabzadeh Baniasadi et al. [57] expressed that among the common minerals, clinopyroxene is considered an important mineral for thermo-barometric estimates, oxygen fugacity, and petrological interpretations, including the type of magma series and the tectonic environment of magma formation, due to its specific chemical composition and high resistance to alteration. Because, first, this mineral contains a wide range of elements present in magma, and in fact, its composition can be interpreted as a proxy of the parental basaltic magma composition. Second, Cpx is present in a wide range of rock compositions (komatiite, picrite, basalt, andesite, dacite, and even some rhyolites and their internal equivalents), and third, it is found in many tectonic environments, from hot spots and intracontinental rifts to mid-ocean ridges, oceanic islands, arc islands, and continental margin magmatic arcs [23].

6.1.1. Whole Rock/Glass Geothermometry

Poutirka [23] recognized that, in spite of the simplicity and narrow calibration range, the Helz and Thornber [58] and Montierth et al. [59] thermometers with very high correlation coefficients) R = 0.91) for both models, work remarkably well for liquid thermometry. The formulations are depending only upon the wt% of MgO in a liquid (MgO^{liq}): T(°C)=20.1MgO^{liq}+1014 °C [58] and T(°C)=23.0MgO^{liq}+1012 °C [59]. According to Helz and Thornber [58], the whole rock thermometry for the Lavarab basanitic lavas is estimated to be 1237-1243 °C (avg=1239 °C) and for the alkaline basaltic lavas to be 1151-1209 °C (avg=1180 °C) independent of pressure. The Putirka [23] equations (13, 14, 15 16) can be applied to glass (liquid) thermometry. Equations (13)-(15) are applicable to any volcanic rock saturated with olivine and any other collection of phases, over the following compositional and P-T range: P = 0.0001-14.4 GPa; T =729-2000 °C; SiO_2 = 31.5-73.64 wt%; Na_2O+K_2O = 0-14.3 wt%; H_2O = 0-18.6 wt%. The equation (16) is similar to Yang et al. [60] equation (4) that applies to liquids in equilibrium with olivine+ plagioclase+ clinopyroxene, but it performs less well for liquids that are

 doi:10.20944/preprints202504.0525.v2

additionally saturated with other phases, such as spinel or other oxides. Using the Putirka [23] equation 13: T(°C)=26.3MgO^{liq}+994.4 °C) the whole rock geothermometry for the basanites is estimated to be 1286-1294 °C (avg=1288.7 °C) and for the alkali basalts to be 1173.5-1249.5 °C (SEE= ±71 °C). Also, the glass thermometry for a group of alkali basalts with a hyalo matrix (L.81, L.38) indicates an average temperature of 1055.5 °C using Helz and Thornber [58] method and 1048.7 ±71 °C using Putirka [23] equation 13 (independent to pressure).

6.1.2. Olivine Geothermometry

When using thermometers or barometers based on equilibrium constants, it is crucial that equilibrium between the phases is achieved. Otherwise, any calculated pressure-temperature condition will be meaningless [23]. For the olivine–liquid thermometer, the composition of whole rock or glass is needed. If the liquid is in equilibrium with the olivine composition, the Fe–Mg exchange coefficient ol-liq is expected to be in the range of KD (Fe-Mg)$^{ol\text{-}liq}$ = 0.30 ± 0.03 [61,62], which means that the thermometer can be applicable to the volcanic system.

The ranges of Fe–Mg exchange coefficients (KD) are from 0.11 to 0.69 for basanites and from 0.27 to 0.33 for alkali basalts. Based on the Rhodes diagram (Figure 10; [63]) olivine is generally in equilibrium with the coexisting liquid in the LABL rocks, except of some in some samples. Petrographic evidences such as absorption and rounded-shape and patchy zoned (in back scattered image) in olivine crystals confirm the disequilibrium between olivine and liquid.

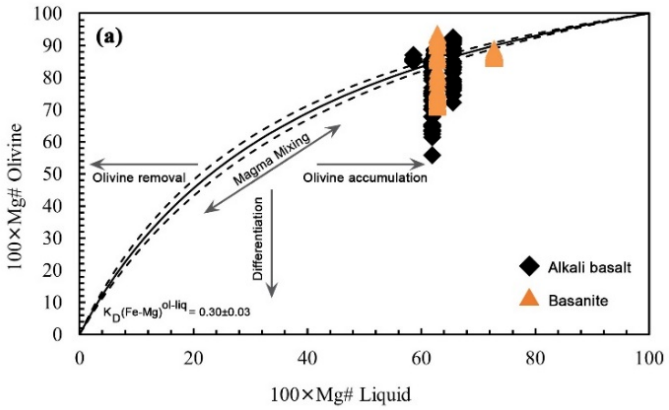

Figure 10. Measured Mg# of Lavarab olivines verses melt Mg# of their host basalts (Rhodes diagram). Equilibrium curves are calculated from the Fe/Mg partition coefficient be-tween olivine and melt. Melt compositions are based on LABL whole-rock.

The thermometers of Putirka et al.'s [31] equations (2) and (4), as reproduced in Putirka [23] equations (21) and (22), with standard error of estimate (SEE) ±53 °C and ±29 °C respectively, is the best estimates when water is present.

Using both above equations and averaging the results at constant pressure (e.g., 1.4 GPa equal with 14 kbar), the crystallization temperature of our acceptable olivine (with KD(Fe-Mg)$^{ol\text{-}liq}$ close to or equal to 0.30 ± 0.03) in this method is calculated 1386-1390 °C for basanites (n = 2), and 1299-1336 °C for alkali basalts (n = 32).

6.1.3. Clinopyroxene Geothermobarometry

Reconstructing the temperature and pressure conditions that control magma crystallization before eruption [23] is a crucial topic in igneous petrology, volcanology, and geochemistry. Clinopyroxene is common mineral in igneous rocks, especially in intermediate to ultrabasic rocks, and shows a wide range of compositional variations. Due to its combined sensitivity to the temperature and pressure prevailing in magma, numerous thermobarometers have been constructed based on clinopyroxene-only [22,45,64] and Clinopyroxene-liquid equilibria [23,46,49,65]. However, Wang et al. [56] state that clinopyroxene-only thermobarometry is one of the most practical tools to reconstruct

 doi:10.20944/preprints202504.0525.v2

crystallization pressures and temperatures of clinopyroxenes. Because it does not require any information of coexisting silicate melt or other co-crystallized mineral phases, it has been widely used to elucidate the physiochemical conditions of crystallizing magmas. In this section, we examine the application of clinopyroxene-based geothermobarometers for the LABL.

In the Seosoo [21] method, which uses all the oxides present in the mineral, temperature estimation is performed based on the calculation of XPT and YPT indices.

Accordingly, the clinopyroxenes of the LABL rocks crystallized at temperatures of about 1150 to 1200 °C for trachy basalt, 1165 to 1270 °C for alkali basalt and 1170 to 1230 °C for basanite and pressures of about 0.3 GPa to 0.6 GPa for trachy basalt, 0.4 to 1.4 GPa for alkali basalt, and 0.5 to 1.25 GPa for basanite (Figure 11).

Putirka [23] equation (32d), another method of single pyroxene thermometry based on Nimis and Taylor [22] clinopyroxene-only thermometer model, is a more precise thermometer.

Using the above equation, the crystalization temperature of clinopyroxenes for the intermediate part of LABL trachy basalt was estimated to be between 1156 and 1223 °C with an average of 1190 °C and a pressure (equation 32b) between 0.13 and 0.9 GPa with an average of 0.51 GPa, for alkali basalts to be between 1135 and 1287 °C with an average of 1209 °C and a pressure between 0.1 and 1.4 GPa with an average of 0.65 GPa, and for basanites to be between 934 and 1278 °C with an average of 1200 °C and a pressure between 0.15 and 1.34 GPa with an average of 0.71 GPa. The results of different geothermobarometry are presented in Table 2 based on clinopyroxene-only composition for three types of Lavarab lavas.

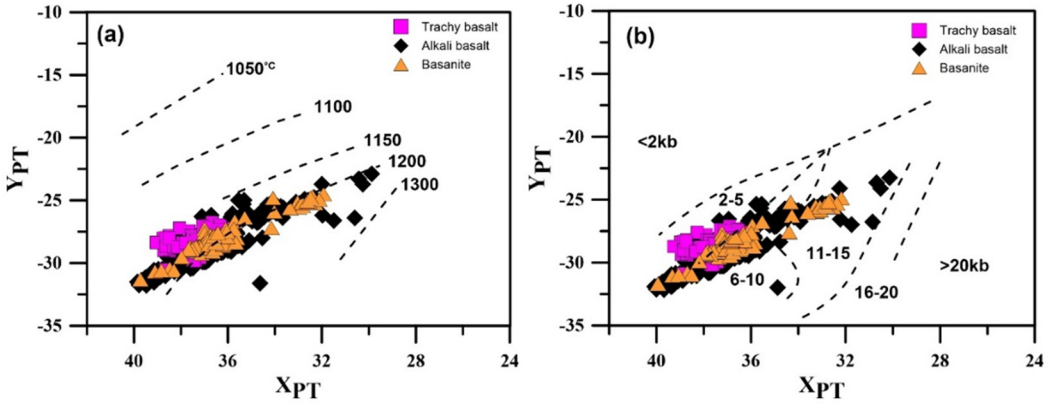

Figure 11. XPT-YPT plot [21] of clinopyroxene crystallization (a) temperature conditions; (b) pressure conditions for Lavarab volcanic rocks.

$XPT = 0.446SiO_2 + 0.187TiO_2 — 0.404Al_2O_3 + 0.346FeO(total) — 0.052MnO + 0.309MgO + 0.431CaO — 0.446Na_2O$

$YPT = -0.369SiO_2 + 0.535TiO_2 — 0.317Al_2O_3 + 0.323FeO(total) + 0.235MnO — 0.516MgO — 0.167CaO — 0.153Na_2O$

Table 2. P-T results of different Cpx-only geothermobarometry models for Lavarab basaltic Lavas.

Clinopyroxene-only Thermobarometry							
	Nimis (1995) (SEE*= ±0.16 GPa)	**Nimis and Ulmer (1998)** (SEE= ±0.15 GPa)	**Seosoo (1997)**		**Putirka (2008) RiMG**		
					Equation (32a) (SEE= ±0.26 GPa)	**Equation (32b)** (SEE= ±0.26 GPa)	**Equation (32d)** (SEE= ±58 °C)
	P (GPa)	**P (GPa)**	**T (°C)**	**P (GPa)**	**P (GPa)**	**P (GPa)**	**T(°C)**
Trachy basalt n = 93	0.007-0.27 (avg=0.11)	0.0024-0.27 (avg=0.1)	1150-1200	0.3-0.6	0.12-0.9 (avg=0.55)	0.13-0.9 (avg=0.51)	1156-1223 (avg=1190)
Alkali basalts n = 418	0.003-1.19 (avg=0.2)	0.002-1.23 (avg=0.2)	1165-1270	0.4-1.45	0.03-1.99 (avg=0.74)	0.1-1.4 (avg=0.65)	1135-1287 (avg=1209)
Basanites	0.003-0.5	0.005-0.52	1170-1230	0.5-1.25	0.1-1.57	0.15-1.34	934-1278

 doi:10.20944/preprints202504.0525.v2

n = 169	(avg=0.19)	(avg=0.18)		(avg=0.8)	(avg=0.71)	(avg=1200)

Over the last thirty years other geothermobarometric methods for estimating the crystallization conditions of a magma chamber is the use of clinopyroxene-liquid equilibrium [23,49,65–70]. Thermobarometry based on clinopyroxene-melt equilibrium is challenging because, often due to the openness of magmatic systems, the crystallization conditions of juvenile clinopyroxene are not in equilibrium with their coexisting melt during magma crystallization, due to processes such as magmatic contamination, magma mixing and mingling, intrusion of new magmatic pulses into the magma chamber, and metasomatism. Pressure is one of the key variables that controls magmatic phase equilibria. However, estimating magma chamber pressures from erupted products is challenging [49]. To use this method, in addition to the mineral composition, one needs the whole rock or glass composition and the equilibrium between both two phases (mineral and melt) is the most important issue in this respect. It means one cannot utilize this method if clinopyroxene and whole rock or glass composition are not in equilibrium with each other, and one can understand it via $KD(Fe\text{-}Mg)^{Cpx\text{-}liq}$. When the Fe–Mg exchange coefficients of clinopyroxene-liquid composition "$KD(Fe\text{-}Mg)^{Cpx\text{-}liq}$" is close or equal to 0.28±0.08 [63], indicating Cpx-liq equilibria. Based on the Rhodes diagram (Figure 12), most clinopyroxenes in each sample are not in equilibrium with the coexisting melt in the Lavarab volcanic rocks. This then implies an open system because of multi pulse melt injections or rapid magma ascent. Petrographic evidences such as sieve texture, absorption, and oscillatory zonation in more clinopyroxene crystals confirm the disequilibrium between clinopyroxene and melt.

The ranges of Fe–Mg exchange coefficients of clinopyroxene-only composition ($KD(Fe\text{-}Mg)^{Cpx}$) are from 0.24 to 0.31 for basanites, but the $KD(Fe\text{-}Mg)^{Cpx\text{-}liq}$ ranging is 0.3 to 1, so there are no eligible data to use this method for basanites in the present case. In alkali basalts, the $KD(Fe\text{-}Mg)^{Cpx}$ is from 0.28 to 0.29 and the $KD(Fe\text{-}Mg)^{Cpx\text{-}liq}$ is 0.24 to 0.29 witch are acceptable ranges to calculate mineral-liquid thermobarometry. In trachy basalt the $KD(Fe\text{-}Mg)^{Cpx}$ is from 0.25 to 0.27 and the $KD(Fe\text{-}Mg)^{Cpx\text{-}liq}$ is 0.1 to 0.23 as well as basanite no eligible data to use Cpx-liq thermobarometry method in our data.

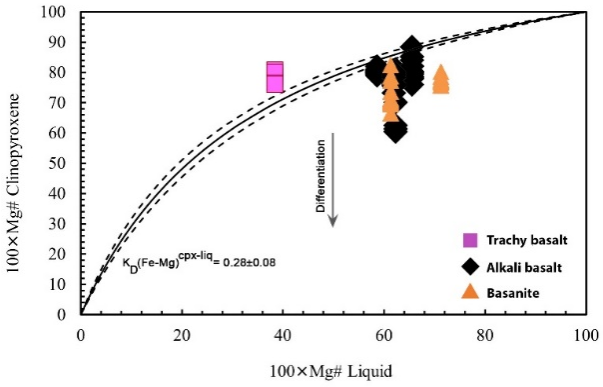

Figure 12. Rhodes diagram, [63], measured Mg# of Lavarab clinopyroxene verses melt Mg# of their host basalts. Equilibrium curves are calculated from the Fe/Mg partition coefficient between clinopyroxene and melt. Melt compositions are based on LABL whole-rock.

Here, published models are used to estimate the temperature and pressure conditions prevailing in the magma chamber during the clinopyroxene crystallization. Using [46] method, the temperature ranges of alkali basalt Cpx crystallization were calculated between 1071 to 1215 °C in a pressure of 0.77-1 GPa (see Table 3). Putirka [23] equation (32c) represents a barometer based on the partitioning of Al between clinopyroxene and liquid.

Based on equation 32c [23], the pressure range for the crystallization of clinopyroxene in alkali basalt was determined to be between 0.55-1.05 GPa and using Putrika [23] equation 33 model, the temperature range for the crystallization of clinopyroxene was estimated to be between 1132 and 1206 °C (refer to Table 3).

 doi:10.20944/preprints202504.0525.v2

Neave and Putirka [49] represent a barometer based on Jd-in-clinopyroxene have been applied to rift zone magmas from Iceland. This method was calibrated from experimental data in the 1 atm to 2 GPa range to improve the accuracy of Jd-in-clinopyroxene barometry at pressures relevant to magma storage in the crust.

Utilizing Neave and Putirka [49] model, the pressure ranging of clinopyroxene crystallization was determined to be between 2.12- 6.7 for alkali basalt (see Table 3).

This section may be divided by subheadings. It should provide a concise and precise description of the experimental results, their interpretation, as well as the experimental conclusions that can be drawn.

Table 3. P-T results of different Cpx-liquid equilibrium geothermobarometry models for LABL.

Clinopyroxene- Whole Rock Equilibrium Thermobarometry					
	Putirka et al. (2003)		**Putirka (2008)**	**Putirka (2008)**	**Neave and Putirka (2017)**
	T (°C)	**P (GPa)**	**P (GPa)**	**T (°C)**	**P (GPa)**
	(SEE*= ±61 °C)	(SEE= ±0.48 GPa)	**Equation (32c)** (SEE= ±0.5 GPa)	**Equation (33)** (SEE= ±46 °C)	(SEE= ±0.14 GPa)
Trachy basalt	N/A	N/A	N/A	N/A	N/A
Alkali basalt n = 15	1071-1215 (avg=1197.8)	0.77-1 (avg=0.87)	0.55-1.05 (avg=0.78)	1132-1206 (avg=1159)	0.21-0.67 (avg=0.44)
Basanite	N/A	N/A	N/A	N/A	N/A

* SEE considering for anhydrous system.

The temperature-pressure modeling for all rock types (Figure 13) is illustrated the P-T binary diagrams using the clinopyroxene-only method and the Wo-En-Fs ternary diagram for the clinopyroxene crystallization temperature ranging, that were drawn by MagMin_PT.

Finally, using clinopyroxene-only thermobarometry, the crystallization temperature of clinopyroxenes in basanite is about 1120–1240 °C at a pressure of 0.2–1.2 GPa, which crystallized at depths of ~7.7–46 km. The clinopyroxene crystallization conditions for alkali basalt are determined in 1110 to 1260 °C and 0.1 to 1.35 GPa at depths of ~3.8 to 51 km, and for trachy basalt, temperatures of 1110 to 1190 °C and low to moderate pressures (0.05 to 0.75 GPa) at depths of 2 to 29 km. However, based on thermobarometry using the clinopyroxene-melt method, for clinopyroxene that are in equilibrium with the melt, the temperature of magma crystallization in alkali basalt is estimated to be about 1071 to 1215 °C at a pressure of 0.55 to 1.05 GPa in a depth of ~21 to 40 km.

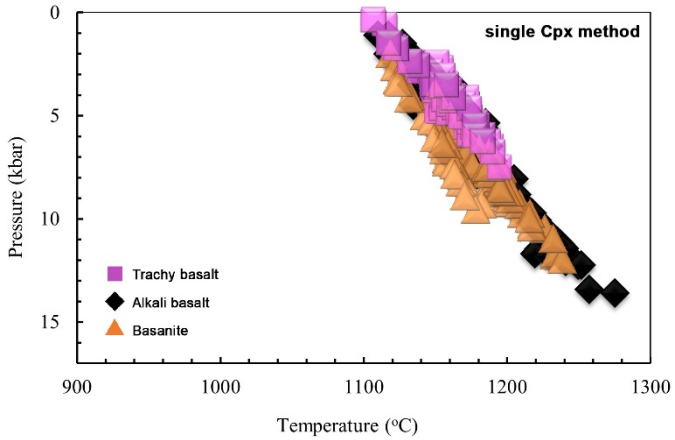

Figure 13. P-T binary diagrams [44], clinopyroxene-only thermobarometry modeling of Lavarab volcanic rocks.

 doi:10.20944/preprints202504.0525.v2

6.2. Magma Crystallization Evolution Modeling

Basaltic magma, due to low viscosity and high temperature, exhibits significant mobility and begins to ascend immediately after generation in the mantle. Because of the lower density and very high viscosity of the continental crust, basaltic magma accumulates beneath the lower crust at the Moho boundary (magmatic underplating) and starts to crystallize (olivine crystallization). If suitable pathways open, the magma can rise through faults and fractures in extensional zones, and crystallization occurs at appropriate depths within magmatic chambers. In another words, minerals get a chance to crystallize and grow when magma, due to its viscosity being the same as the host rock, refuses to rise and stops in the crust, creating magma chambers (For example, the clinopyroxene mega-phenocrysts in LABL indicate periods of crystallization occurred in a semi-deep magma chamber(s) during the ascent of magma from the mantle to the surface). However, because of the low viscosity, high temperature, and origin from deeper depths, basaltic magmas frequently reach the Earth's surface, forming basalt flows rather than appearing as gabbroic masses. Based on the temperature-pressure estimates processed in this study, the parental basaltic magma that formed the Neogene basaltic rocks of Lavarab, is ascended after generation in the mantle and accumulated at depths exceedingly approximately 45 kilometers (Moho depth in east of Iran [71,72]) in the lower crust, and initiated crystallization of olivine, apatite, magnetite, and clinopyroxene.

When the channel or conduit is opened for ascending, the basaltic magma reached depths between 30 to 10 km (middle crust) and underwent the main and significant crystallization phase in the magmatic chambers at these depths (crystallization of plagioclase and clinopyroxene). Then, as the magma continues its ascent and reaches depths less than 10 kilometers (upper crust), the final stage of deep crystallization occurred. Eventually, the remaining magma, along with the phenocrysts, rises through fractures and faults to extrude. In the case of rocks with a glassy matrix and prismatic structure, it can be said that magma probably passed from the middle crust to the upper crust without stopping and flowed through a passageway created by a tensile mechanism resulting from the action of dextral faults in the area (Figure 14).

 doi:10.20944/preprints202504.0525.v2

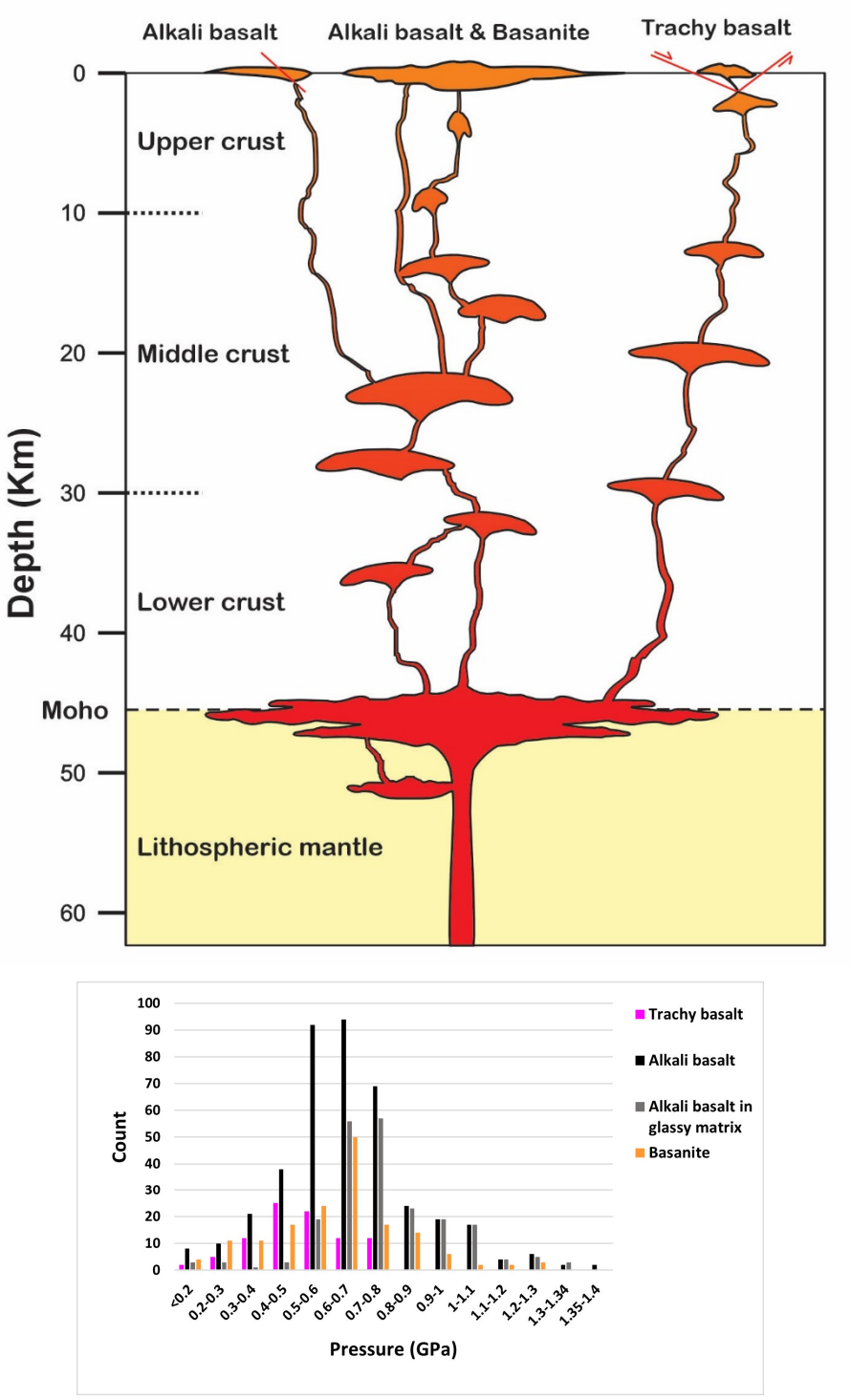

Figure 14. Schematic illustration of the magma plumbing system of the Lavarab lavas. Determination of magma chamber depths are Limited to clinopyroxene pressure frequency. Pressure is calculated by Putirka equation 32b [23].

To find out the temperature and pressure differences between mega-phenocrysts and phenocrysts, in terms of only- clinopyroxene thermobarometry, one sample belonging to alkali basalts in glassy matrix (L.81) was selected. As can be seen in Figure 15, the maximum temperature estimated for mega-phenocrysts is ~1200 °C at the maximum pressure of ~1 GPa, while the maximum temperature for phenocrysts is ~1190 °C at the maximum pressure of ~0.7 GPa. In other words, the crystallization of clinopyroxene mega-phenocrysts and clinopyroxene phenocrysts started at depths of ~38 km and ~26 km, in lower crust and middle crust respectively for this sample. There is no significant temperature decrease over the 0.3 GPa pressure release that shows the none stop rapid ascent from

 doi:10.20944/preprints202504.0525.v2

depths of ~11 km (middle crust-upper crust boundary) to the surface, and resulting in the glassy matrix for this sample. This could be due to the magma reservoir being fed by new melt injections, thus pressurizing the magma chamber, opening the ascent path by faults and fractures, high temperature and the low viscosity of the magma compared to the host rocks throughout the eruption path.

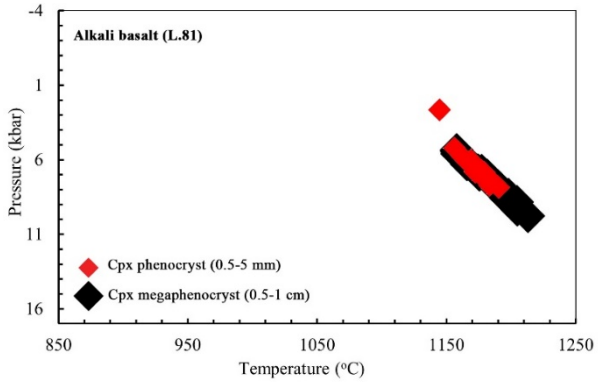

Figure 15. Comparison of the conditions governing the crystallization of clinopyroxene mega-phenocrysts and phenocrysts from the alkali basaltic sample (L.81), based on only- clinopyroxene thermobarometry.

6.3. Magma Type and Tectonic Setting Based on Clinopyroxene Composition

Many metamorphosed and weathered basalts contain fresh clinopyroxene crystals set in an altered groundmass. Microprobe analysis of these relict grains can be used to identify the magma type of the host lava [13]. According to Le Bas [73], the amounts of Al and Ti in the structural framework of pyroxenes depend on the alkalinity of the magma. By utilizing Al_2O_3 and SiO_2 contents in the chemical composition of pyroxenes, it is possible to distinguish alkaline, peralkaline, and subalkaline magma types. In this diagram, the clinopyroxenes of the Oligocene-Miocene LABL fall within peralkaline (for basanite and some alkali basalt) and alkaline-subalkaline ranges (alkali basalt and trachy basalt) (Figure 16a). In the diagram of Ti versus Na+Ca [12], Basanite and alkali basalt are located in the alkali basalt field, but trachy basalt is plotted on sub-alkali basalt-Alkali basalt boundary (Figure 16b).

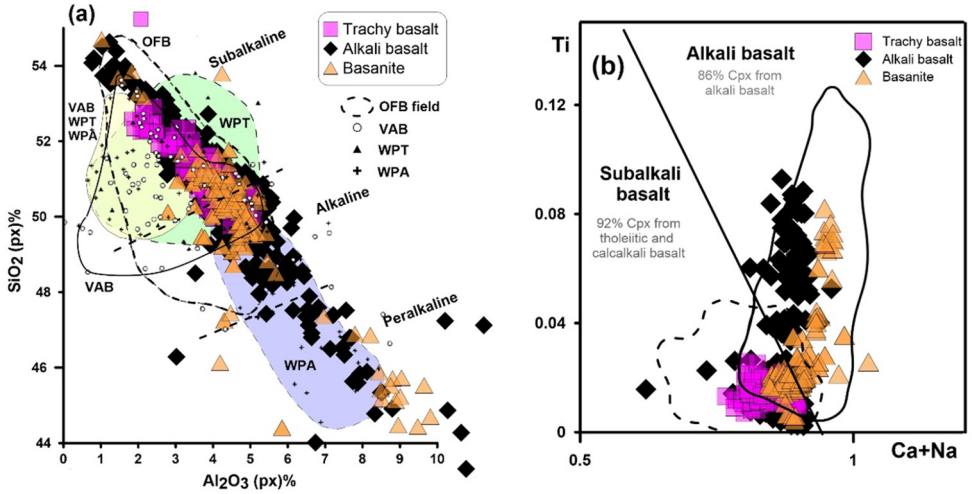

Figure 16. (a) Al_2O_3 versus SiO_2 diagram [13]; (b) Ti versus Na+Ca, discrimination diagram for clinopyroxene phenocrysts from alkali basalts and other basalts [12].

According to Nisbet and Pearce [13], pyroxenes of within plate alkali basalts have high Na and Ti and low Si contents, and pyroxenes of within plate tholeiites and volcanic arc basalts contain more Ti, Fe and Mn. Tholeiitic basalts erupted within plates in oceanic islands or continental rifts (WPT samples), and alkali basalts erupted within plates (WPA samples) [13]. The pyroxene composition

 doi:10.20944/preprints202504.0525.v2

and based on discriminant functions (F1-F2) well distinguishes between alkaline basalts in intra-plate settings (WPA), within-plate tholeiitic magmas (WPT), and volcanic arc basalts (VAB) from one another. However, a significant overlap observed between within-plate tholeiites and oceanic floor basalts (WPT-OFB), as well as between volcanic arc basalts and oceanic floor basalts (VAB-OFB) exists. In this diagram, trachy basalt and alkali basalt are located within the range of volcanic arc basalts (VAB), but basanite is located in within plate alkali basalt. Also, diagram of pyroxene composition based on Na_2O-MnO-TiO_2 and TiO_2-SiO_2 provide the basis for visual discrimination [13]. In Na_2O-MnO-TiO_2 diagram, basanite and alkali basalt is located within WPA field and trachy basalt is plotted in VAB+WPA field. In TiO_2-SiO_2 discrimination diagram, trachy basalt, alkali basalt and basanite are located within the WPA and to some extent in the VAB (Figure 17a,b,c). Also, Houshmand-Mananvi et al. [42] showed that the Oligocene-Miocene LABL based on whole rock chemistry are related to the post continental collision and within-plate tectonic setting, but sometimes indicated unreal active margin tectonic setting. Probably, some parts of the mantle were metasomatized by released fluids from the Sistan oceanic lithosphere subduction resulting in a distinct mantle heterogeneity. According to Leterrier et al. [12], the clinopyroxenes of trachy basalt and alkali basalt are similar to clinopyroxenes from orogenic tholeiitic basalt using Ti and Ca cations, while the Ti and Ca contents of clinopyroxene in basanite is similar to clinopyroxene from alkali basalt (Figure 17d). Also, according to Houshmand-Mananvi et al. [42] based on whole rock chemistry, the studied LABL are associated with post-collisional continental environments characterized by an intraplate (WPA) tectonic setting. These lavas occasionally exhibit features indicative of a pseudo-active margin (VAB), attributed to mantle metasomatism caused by fluids released during the subduction of the Sistan oceanic lithosphere (Late Cretaceous- Middle Eocene, [2,41]). This subduction process generated mantle heterogeneity through the introduction of fluids into portions of the mantle.

The oxygen fugacity (fO_2) is a convenient monitor of oxidation state of melts. The oxidation state of a melt is a critical controlling parameter of magmatic processes as it controls the iron redox state of the melt [69,74–77], and it strongly influences the crystallization sequences and the composition of crystallizing minerals [78]. Iron is the main element that is readily oxidized or reduced in response to the range of redox states experienced by crustal rocks [79–83]. The amount of ferric (Fe^{3+}) iron is commonly a good indicator of the redox budget of a rock [84], and the ratio of ferric to ferrous (Fe^{2+}) iron provides a first-order indication of its oxidation state [85]. The oxidation state of the experimental charge is calibrated by solid mineral buffers that are expected to fix aO_2 (oxygen activity) for the duration of the experiment [86]. The most widely used buffers, in order of increasing aO_2, are iron–quartz–fayalite (IQF), iron–(wüstite)–magnetite, quartz–fayalite–magnetite (QFM), Ni–NiO (NNO), Mn1-xO–Mn_3O_4, hematite–magnetite (HM), Mn_3O_4–Mn_2O_3 and Mn_2O_3–MnO_2 (e.g., [87]). The oxidation states experienced by most crustal rocks are considered to be approximately bracketed by QFM and HM (e.g., [88]). The ferric iron content of the pyroxenes is shown on a plot (Figure 17e) of charge deficiencies vs. charge excesses relative to a pyroxene of charge balanced composition [16]. Na in the pyroxene M2 site and Al in a tetrahedral site are charge deficiencies relative to “Quad”, and Al, Cr^{3+}, Fe^{3+}, and Ti^{4+} in octahedral sites are charge excesses. In Figure 17e, lateral displacement of points to the left of the line Fe^{3+}=0 indicates the relative amount of ferric iron present [16], reflecting more oxidizing conditions and high oxygen fugacity during pyroxene crystallization for LABL.

According to the diagram presented by Aoki and Shiba [89], the pyroxenes of the LABL are primarily formed at low to moderate pressures. This indicates that the essential crystallization of pyroxenes occurred during the ascent from depth to the surface in an environment characterized by varying pressures, ranging from the moderate pressure prevailing in the middle crust to the lower pressure in the upper crust (Figure 17f).

 doi:10.20944/preprints202504.0525.v2

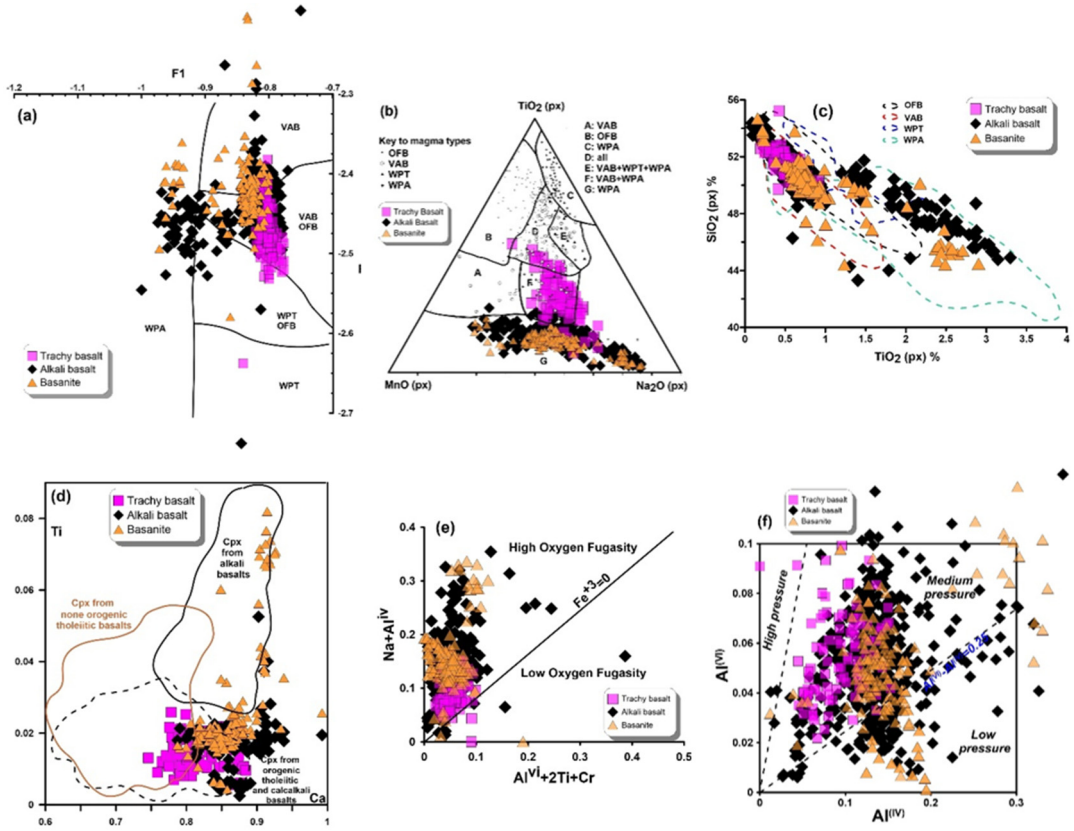

Figure 17. Various discrimination diagrams based on the compositional of clinopyroxenes from Nisbet and Pearce [13] for the basaltic lavas of Lavarab. (a) Diagram of F1-F2; (b) diagram of Na_2O-MnO-TiO_2; (c) diagram of TiO_2-SiO_2. (d) Diagram based on clinopyroxene Ca-Ti cations [12]; (e) Oxidizing conditions during pyroxene crystallization [16]; (f) Plot of AlIV versus AlVI of pyroxene to pressure determination [89].

$F1=-0.012*SiO_2-0.0807*TiO_2+0.0026*Al_2O_3-0.0012*FeO^*-0.0026*MnO+0.0087*MgO-0.0128*CaO-0.0419*Na_2O$

$F2=-0.0469*SiO_2-0.0818*TiO_2-0.0212*Al_2O_3-0.0041*FeO^*-0.1435*MnO-0.0029*MgO+0.0085*CaO+ 0.016*Na_2O$

7. Conclusions

The mineral chemistry of the Neogene basaltic rocks in Lavarab indicates a peralkaline to sub-alkaline magma nature within an intra-plate tectonic setting and volcanic arc environment, which is consistent with the results of whole-rock geochemistry studies on major and trace elements in the region. In examining the conditions of magma crystallization, it was determined that the magma crystallized under conditions of high oxygen fugacity. Also, the different thermobarometry based on glass, whole rock, olivine and clinopyroxene chemistry were used based on the only-mineral and mineral-liquid equilibrium thermobarometry methods. The results are as follows:

1. The whole rock geothermometry for the basanites are estimated to be 1286-1294 °C and for the alkali basalts to be 1173.5-1249.5 °C (SEE= ±71 °C, independent to pressure).
2. The glass thermometry for alkali basalts is calculated 1048.7 ±71 °C independent to pressure.
3. The olivine-liquid thermometry obtained 1380-1390 °C for basanites, and 1299-1336 °C for alkali basalts at a constant pressure of 1.4 GPa.
4. Using different thermobarometry methods based on single clinopyroxene chemistry indicates magma crystallization for bazanite in ~1120–1240 °C at ~0.2–1.2 GPa, at depths of ~7.7–46 km. The clinopyroxene crystallization conditions for alkali basalt are determined in about 1110 to 1260 °C and 0.1 to 1.35 GPa at depths of ~3.8 to 51 km, and for trachy basalt, at temperatures of 1110 to 1190 °C and low to moderate pressures (0.05 to 0.75 GPa) at depths of 2 to 29 km.

 doi:10.20944/preprints202504.0525.v2

5. The single pyroxene thermobarometry, as the most practical method, illustrate some magma storages from lower crust to upper crust for basanites and alkali basalts, while trachy basalts are related to magma chambers located in middle crust to upper crust. Also, the chemical compositions of phenocrysts in the studied basaltic lavas reflect evidence of magma recharge through multi pulses of new magma injected into the existing reservoir prior to eruptions.
6. The relative amount of ferric iron present reflects more oxidizing conditions and high oxygen fugacity during pyroxene crystallization for LABL.

Author Contributions: Conceptualization, Sara Houshmand-Mananvi and Mehdi Rezaei-Kahkhaei; Data curation, Sara Houshmand-Mananvi; Formal analysis, Sara Houshmand-Mananvi; Investigation, Sara Houshmand-Mananvi and Habibollah Ghasemi; Methodology, Sara Houshmand-Mananvi, Habibollah Ghasemi and Urs Klötzli; Software, Sara Houshmand-Mananvi; Supervision, Mehdi Rezaei-Kahkhaei; Visualization, Sara Houshmand-Mananvi; Writing—original draft, Sara Houshmand-Mananvi; Writing—review & editing, Sara Houshmand-Mananvi, Mehdi Rezaei-Kahkhaei and Urs Klötzli.

Data availability: Data will be made available on request. Requests can be directed to the corresponding author(s).

Acknowledgments: This study is a part of the PhD thesis by the first author and funded by Ministry of Science, Research and Technology, Iran. The authors appreciate Fatemeh Vakili, Mehdi Nowrouzi and Hasan Narimani (Geological Survey of Iran, Tehran, Iran) due to micro-paleontological studies. The authors are grateful to Ewa Krzemińska and Grzegorz Zieliński (Polish Geological Institute, Warsaw, Poland) helping us to do the EPMA analysis and to Christian Ball (University of Vienna, Vienna, Austria) helped with the SEM images. Thanks to Mohammad Goudarzi due to help in data-Curation and software, and also Sima Houshmand-Manavi due to contribution map preparation, data-Curation and visualization. Thank are also due to editor-in-chief of the journal, associated editor and reviewers of the journal for their review and handling of this paper.

Conflicts of Interest: The authors declare no conflicts of interest.

Abbreviations

The following abbreviations are used in this manuscript:

LABL	Lavarab Alkaline Basaltic Lavas
GSI	Geological Survey of Iran

References

1. Camp, V.E.; Griffis, R.J. Character, Genesis and Tectonic Setting of Igneous Rocks in the Sistan Suture Zone, Eastern Iran. *Lithos* **1982**, *15*, 221–239. https://doi.org/10.1016/0024-4937(82)90014-7.
2. Tirrul, R.; Bell, I.R.; Griffis, R.J.; Camp, V.E. The Sistan Suture Zone of Eastern Iran. *GSA Bulletin* **1983**, *94*, 134–150. https://doi.org/10.1130/0016-7606(1983)94<134:TSSZOE>2.0.CO;2.
3. Pang, K.-N.; Chung, S.-L.; Zarrinkoub, M.H.; Mohammadi, S.S.; Yang, H.-M.; Chu, C.-H.; Lee, H.-Y.; Lo, C.-H. Age, Geochemical Characteristics and Petrogenesis of Late Cenozoic Intraplate Alkali Basalts in the Lut–Sistan Region, Eastern Iran. *Chemical Geology* **2012**, *306–307*, 40–53. https://doi.org/10.1016/j.chemgeo.2012.02.020.
4. Pang, K.-N.; Chung, S.-L.; Zarrinkoub, M.H.; Khatib, M.M.; Mohammadi, S.S.; Chiu, H.-Y.; Chu, C.-H.; Lee, H.-Y.; Lo, C.-H. Eocene–Oligocene Post-Collisional Magmatism in the Lut–Sistan Region, Eastern Iran: Magma Genesis and Tectonic Implications. *Lithos* **2013**, *180–181*, 234–251. https://doi.org/10.1016/j.lithos.2013.05.009.
5. Mohammadi, A.; Burg, J.-P.; Bouilhol, P.; Ruh, J. U–Pb Geochronology and Geochemistry of Zahedan and Shah Kuh Plutons, Southeast Iran: Implication for Closure of the South Sistan Suture Zone. *Lithos* **2016**, *248–251*, 293–308. https://doi.org/10.1016/j.lithos.2016.02.003.

 doi:10.20944/preprints202504.0525.v2

6. Bröcker, M.; Hövelkröger, Y.; Fotoohi Rad, G.; Berndt, J.; Scherer, E.E.; Kurzawa, T.; Moslempour, M.E. The Magmatic and Tectono-Metamorphic History of the Sistan Suture Zone, Iran: New Insights into a Key Region for the Convergence between the Lut and Afghan Blocks. *Journal of Asian Earth Sciences* **2022**, *236*, 105313. https://doi.org/10.1016/j.jseaes.2022.105313.
7. Biabangard, H.; Sepidbar, F.; Palin, R.M.; Boomeri, M.; Whattam, S.A.; Homam, S.M.; Shahraki, O.B. Neogene Calc-Alkaline Volcanism in Bobak and Sikh Kuh, Eastern Iran: Implications for Magma Genesis and Tectonic Setting. *Miner Petrol* **2023**, *117*, 63–77. https://doi.org/10.1007/s00710-022-00798-8.
8. Behruzi, A. Geological Quadrangle Map of Zahedan 1973.
9. Aghanabati, A. Geological map of Kuh-e Do Poshti 1987.
10. Aghanabati, A. Geological quadrangle map of Daryacheh-Ye-Hamun 1991.
11. Gill, R. *Igneous Rocks and Processes: A Practical Guide*; Wiley-Blackwell, 2010; ISBN 978-1-4443-3065-6.
12. Leterrier, J.; Maury, R.C.; Thonon, P.; Girard, D.; Marchal, M. Clinopyroxene Composition as a Method of Identification of the Magmatic Affinities of Paleo-Volcanic Series. *Earth and planetary science letters* **1982**, *59*, 139–154.
13. Nisbet, E.G.; Pearce, J.A. Clinopyroxene Composition in Mafic Lavas from Different Tectonic Settings. *Contrib. Mineral. and Petrol.* **1977**, *63*, 149–160. https://doi.org/10.1007/BF00398776.
14. Wood, B.J.; Banno, S. Garnet-Orthopyroxene and Orthopyroxene-Clinopyroxene Relationships in Simple and Complex Systems. *Contr. Mineral. and Petrol.* **1973**, *42*, 109–124. https://doi.org/10.1007/BF00371501.
15. Wells, P.R.A. Pyroxene Thermometry in Simple and Complex Systems. *Contr. Mineral. and Petrol.* **1977**, *62*, 129–139. https://doi.org/10.1007/BF00372872.
16. Schweitzer, E.L.; Papike, J.J.; Bence, A.E. Statistical Analysis of Clinopyroxenes from Deep-Sea Basalts. *American Mineralogist* **1979**, *64*, 501–513.
17. Lindsley, D.H. Pyroxene Thermometry. *American Mineralogist* **1983**, *68*, 477–493.
18. Davidson, P.M. Thermodynamic Analysis of Quadrilateral Pyroxenes. Part 1: Derivation of the Ternary Nonconvergent Site-Disorder Model. *Contr. Mineral. and Petrol.* **1985**, *91*, 383–389. https://doi.org/10.1007/BF00374694.
19. Davidson, P.M.; Lindsley, D.H. Thermodynamic Analysis of Quadrilateral Pyroxenes. Part II: Model Calibration from Experiments and Applications to Geothermometry. *Contr. Mineral. and Petrol.* **1985**, *91*, 390–404. https://doi.org/10.1007/BF00374695.
20. Bertrand, P.; Mercier, J.-C.C. The Mutual Solubility of Coexisting Ortho- and Clinopyroxene: Toward an Absolute Geothermometer for the Natural System? *Earth and Planetary Science Letters* **1985**, *76*, 109–122. https://doi.org/10.1016/0012-821X(85)90152-9.
21. Soesoo, A. A Multivariate Statistical Analysis of Clinopyroxene Composition: Empirical Coordinates for the Crystallisation PT-estimations. *GFF* **1997**, *119*, 55–60. https://doi.org/10.1080/11035899709546454.
22. Nimis, P.; Taylor, W.R. Single Clinopyroxene Thermobarometry for Garnet Peridotites. Part I. Calibration and Testing of a Cr-in-Cpx Barometer and an Enstatite-in-Cpx Thermometer. *Contrib Mineral Petrol* **2000**, *139*, 541–554. https://doi.org/10.1007/s004100000156.
23. Putirka, K.D. Thermometers and Barometers for Volcanic Systems. *Reviews in Mineralogy and Geochemistry* **2008**, *69*, 61–120. https://doi.org/10.2138/rmg.2008.69.3.
24. Wieser, P.E.; Kent, A.J.R.; Till, C.B.; Donovan, J.; Neave, D.A.; Blatter, D.L.; Krawczynski, M.J. Barometers Behaving Badly I: Assessing the Influence of Analytical and Experimental Uncertainty on Clinopyroxene Thermobarometry Calculations at Crustal Conditions. *Journal of Petrology* **2023**, *64*, egac126. https://doi.org/10.1093/petrology/egac126.
25. Xu, R.; Liu, Y. Al-in-Olivine Thermometry Evidence for the Mantle Plume Origin of the Emeishan Large Igneous Province. *Lithos* **2016**, *266–267*, 362–366. https://doi.org/10.1016/j.lithos.2016.10.016.
26. Herzberg, C. Basalts as Temperature Probes of Earth's Mantle. *Geology* **2011**, *39*, 1179–1180. https://doi.org/10.1130/focus122011.1.
27. Herzberg, C.; Asimow, P.D. PRIMELT3 MEGA. XLSM Software for Primary Magma Calculation: Peridotite Primary Magma MgO Contents from the Liquidus to the Solidus. *Geochemistry, Geophysics, Geosystems* **2015**, *16*, 563–578. https://doi.org/10.1002/2014GC005631.

 doi:10.20944/preprints202504.0525.v2

28. Zhang, L.; Hong, L.-B.; Qian, S.-P.; He, P.-L.; He, M.-H.; Yang, Y.-N.; Wang, J.-T.; Zhang, Y.-Q.; Ren, Z.-Y. The Effect of Elemental Diffusion on the Application of Olivine-Composition-Based Magmatic Thermometry, Oxybarometry, and Hygrometry: A Case Study of Olivine Phenocrysts from the Jiagedaqi Basalts, Northeast China. *American Mineralogist* **2023**, *108*, 1449–1460. https://doi.org/10.2138/am-2022-8567.
29. Herzberg, C.; Asimow, P.D.; Arndt, N.; Niu, Y.; Lesher, C.M.; Fitton, J.G.; Cheadle, M.J.; Saunders, A.D. Temperatures in Ambient Mantle and Plumes: Constraints from Basalts, Picrites, and Komatiites. *Geochemistry, Geophysics, Geosystems* **2007**, *8*. https://doi.org/10.1029/2006GC001390.
30. Herzberg, C.; O'Hara, M.J. Plume-Associated Ultramafic Magmas of Phanerozoic Age. *Journal of Petrology* **2002**, *43*, 1857–1883. https://doi.org/10.1093/petrology/43.10.1857.
31. Putirka, K.D.; Perfit, M.; Ryerson, F.J.; Jackson, M.G. Ambient and Excess Mantle Temperatures, Olivine Thermometry, and Active vs. Passive Upwelling. *Chemical Geology* **2007**, *241*, 177–206. https://doi.org/10.1016/j.chemgeo.2007.01.014.
32. Coogan, L.A.; Saunders, A.D.; Wilson, R.N. Aluminum-in-Olivine Thermometry of Primitive Basalts: Evidence of an Anomalously Hot Mantle Source for Large Igneous Provinces. *Chemical Geology* **2014**, *368*, 1–10. https://doi.org/10.1016/j.chemgeo.2014.01.004.
33. Falloon, T.J.; Danyushevsky, L.V.; Ariskin, A.; Green, D.H.; Ford, C.E. The Application of Olivine Geothermometry to Infer Crystallization Temperatures of Parental Liquids: Implications for the Temperature of MORB Magmas. *Chemical Geology* **2007**, *241*, 207–233. https://doi.org/10.1016/j.chemgeo.2007.01.015.
34. Şengör, A.M.C.; Altıner, D.; Cin, A.; Ustaömer, T.; Hsü, K.J. Origin and Assembly of the Tethyside Orogenic Collage at the Expense of Gondwana Land. *Geological Society, London, Special Publications* **1988**, *37*, 119–181. https://doi.org/10.1144/GSL.SP.1988.037.01.09.
35. Berberian, M. *Generalized Tectonic Map of Iran. In Berberian M (Ed) Continental Deformation in the Iranian Plateau*; Geological Survey of Iran, 1983;
36. Dewey, J.F. Suture Zone Complexities: A Review. *Tectonophysics* **1977**, *40*, 53–67. https://doi.org/10.1016/0040-1951(77)90029-4.
37. Damani Gol, Sh.; Bagheri, S. Paleogene Thrust system in the Eastern Iranian Ranges.; Kharazmi University, Tehran, 2021.
38. Ghassemi, M.R.; Aghanabati, A.; Saeidi, A. Orogenic and epeirogenic events in Iran. ,*33* ,**2023** علوم زمین 106–87. https://doi.org/10.22071/gsj.2022.324032.1970.
39. Sadeghiyan, M. Magmatism, Metallogeny and Emplacement Mechanism of Zahedan Granitoid, science faculty, Tehran University: Tehran, Iran, 2004.
40. Ghasemi, H.; Sadeghian, M.; Kord, M.; Khanslizadeh, A. The evolution mechanism's of Zahedan granitoidic batholith, southeast Iran. *Iranian Journal of Crystallography and Mineralogy* **2010**, *17*, 551–578.
41. Rezaei-Kahkhaei, M.; Corfu, F.; Galindo, C.; Rahbar, R.; Ghasemi, H. Adakite Genesis and Plate Convergent Process: Constraints from Whole Rock and Mineral Chemistry, Sr, Nd, Pb Isotopic Compositions and U-Pb Ages of the Lakhshak Magmatic Suite, East Iran. *Lithos* **2022**, *426–427*, 106806. https://doi.org/10.1016/j.lithos.2022.106806.
42. Houshmand-Mananvi, S.; Rezaei-Kahkhaei, M.; Ghasemi, H. Whole Rock Geochemistry and Tectonic Setting of Oligocene-Miocene Lavarab Lava (North Zahedan). *Scientific Quarterly Journal of Geosciences 34*, 67–86. https://doi.org/10.22071/gsj.2024.460225.2144.
43. Rezaei-Kahkhaei, M.; Esmaeily, D.; Sahraei, H. Evaluation of Impact Processes in the Formation of Neshveh Volcanic Rocks, NW Saveh. *Scientific Quarterly Journal of Geosciences* **2018**, *28*, 285–294. https://doi.org/10.22071/gsj.2017.91461.1190.
44. Gündüz, M.; Asan, K. MagMin_PT: An Excel-Based Mineral Classification and Geothermobarometry Program for Magmatic Rocks. *MinMag* **2023**, *87*, 1–9. https://doi.org/10.1180/mgm.2022.113.
45. Nimis, P. A Clinopyroxene Geobarometer for Basaltic Systems Based on Crystal-Structure Modeling. *Contrib Mineral Petrol* **1995**, *121*, 115–125. https://doi.org/10.1007/s004100050093.
46. Putirka, K.D.; Mikaelian, H.; Ryerson, F.; Shaw, H. New Clinopyroxene-Liquid Thermobarometers for Mafic, Evolved, and Volatile-Bearing Lava Compositions, with Applications to Lavas from Tibet and the Snake River Plain, Idaho. *American Mineralogist* **2003**, *88*, 1542–1554. https://doi.org/10.2138/am-2003-1017.

 doi:10.20944/preprints202504.0525.v2

47. Putirka, K.; Ryerson, F.J.; Mikaelian, H. New Igneous Thermobarometers for Mafic and Evolved Lava Compositions, Based on Clinopyroxene + Liquid Equilibria. *Am Mineral* **2003**, *88*, 1542–1554.
48. Yavuz, F. WinPyrox: A Windows Program for Pyroxene Calculation Classification and Thermobarometry. *American Mineralogist* **2013**, *98*, 1338–1359. https://doi.org/10.2138/am.2013.4292.
49. Neave, D.A.; Putirka, K.D. A New Clinopyroxene-Liquid Barometer, and Implications for Magma Storage Pressures under Icelandic Rift Zones. *American Mineralogist* **2017**, *102*, 777–794. https://doi.org/10.2138/am-2017-5968.
50. Winchester, J.A.; Floyd, P.A. Geochemical Discrimination of Different Magma Series and Their Differentiation Products Using Immobile Elements. *Chemical Geology* **1977**, *20*, 325–343. https://doi.org/10.1016/0009-2541(77)90057-2.
51. Peate, D.W.; Hawkesworth, C.J. Lithospheric to Asthenospheric Transition in Low-Ti Flood Basalts from Southern Paraná, Brazil. *Chemical Geology* **1996**, *127*, 1–24. https://doi.org/10.1016/0009-2541(95)00086-0.
52. Simon, S.B.; Sutton, S.R. Valences of Ti, Cr, and V in Apollo 17 High-Ti and Very Low-Ti Basalts and Implications for Their Formation. *Meteoritics & Planetary Science* **2018**, *53*, 2138–2154. https://doi.org/10.1111/maps.13123.
53. Wilson, M. *Igneous Petrogenesis*; Springer Netherlands: Netherlands, 1989;
54. Morimoto, N.; Kitamura, M. Q-J Diagram for Classification Ofpyroxenes. *Joumal ofthe Japanese Association ofMineralogy, Petrology and Economical Geolog 78*.
55. Morimoto, N.; Fabrise, J.; Ferguson, A.; Ginzburg, I.V.; Ross, M.; Seifert, F.A.; Zussman, J.; Akoi, K.; Gottardi, G. Nomenclature of Pyroxenes. *American Mineralogist 173*, 1123–1133.
56. Wang, X.; Hou, T.; Wang, M.; Zhang, C.; Zhang, Z.; Pan, R.; Marxer, F.; Zhang, H. A New Clinopyroxene Thermobarometer for Mafic to Intermediate Magmatic Systems. *European Journal of Mineralogy* **2021**, *33*, 621–637. https://doi.org/10.5194/ejm-33-621-2021.
57. Arabzadeh Baniasadi, M.; Ghasemi, H.; Angiboust, S.; Rezaei Kahkhaei, M.; Papadopoulou, L. Application of clinopyroxene geothermobarometers on the gabbro/dioritic rocks associated with the Gowd-e-Howz (Siah-Kuh) granitoid stock, Baft, Kerman. *Scientific Quarterly Journal of Geosciences* **2024**, *34*, 117–134. https://doi.org/10.22071/gsj.2024.445550.2136.
58. Helz, R.T.; Thornber, C.R. Geothermometry of Kilauea Iki Lava Lake, Hawaii. *Bull Volcanol* **1987**, *49*, 651–668. https://doi.org/10.1007/BF01080357.
59. Montierth, C.; Johnston, A.D.; Cashman, K.V. An Empirical Glass-Composition-Based Geothermometer for Mauna Loa Lavas. In *Mauna Loa Revealed: Structure, Composition, History, and Hazards*; American Geophysical Union (AGU), 1995; pp. 207–217 ISBN 978-1-118-66433-9.
60. Yang, H.-J.; Frey, F.A.; Clague, D.A.; Garcia, M.O. Mineral Chemistry of Submarine Lavas from Hilo Ridge, Hawaii: Implications for Magmatic Processes within Hawaiian Rift Zones. *Contrib Mineral Petrol* **1999**, *135*, 355–372. https://doi.org/10.1007/s004100050517.
61. Roeder, P.L.; Emslie, R.F. Olivine-Liquid Equilibrium. *Contr. Mineral. and Petrol.* **1970**, *29*, 275–289. https://doi.org/10.1007/BF00371276.
62. Toplis, M.J. The Thermodynamics of Iron and Magnesium Partitioning between Olivine and Liquid: Criteria for Assessing and Predicting Equilibrium in Natural and Experimental Systems. *Contrib Mineral Petrol* **2005**, *149*, 22–39. https://doi.org/10.1007/s00410-004-0629-4.
63. Rhodes, J.M.; Dungan, M.A.; Blanchard, D.P.; Long, P.E. Magma Mixing at Mid-Ocean Ridges: Evidence from Basalts Drilled near 22° N on the Mid-Atlantic Ridge. *Tectonophysics* **1979**, *55*, 35–61. https://doi.org/10.1016/0040-1951(79)90334-2.
64. Nimis, P.; Ulmer, P. Clinopyroxene Geobarometry of Magmatic Rocks Part 1: An Expanded Structural Geobarometer for Anhydrous and Hydrous, Basic and Ultrabasic Systems. *Contrib Mineral Petrol* **1998**, *133*, 122–135. https://doi.org/10.1007/s004100050442.
65. Putirka, K.; Johnson, M.; Kinzler, R.; Longhi, J.; Walker, D. Thermobarometry of Mafic Igneous Rocks Based on Clinopyroxene-Liquid Equilibria, 0–30 Kbar. *Contrib Mineral Petrol* **1996**, *123*, 92–108. https://doi.org/10.1007/s004100050145.

66. Tormey, D.R.; Grove, T.L.; Bryan, W.B. Experimental Petrology of Normal MORB near the Kane Fracture Zone: 22°–25° N, Mid-Atlantic Ridge. *Contr. Mineral. and Petrol.* **1987**, *96*, 121–139. https://doi.org/10.1007/BF00375227.
67. Berndt, J.; Koepke, J.; Holtz, F. An Experimental Investigation of the Influence of Water and Oxygen Fugacity on Differentiation of MORB at 200 MPa. *Journal of Petrology* **2005**, *46*, 135–167. https://doi.org/10.1093/petrology/egh066.
68. Thy, P.; Lesher, C.E.; Nielsen, T.F.D.; Brooks, C.K. Experimental Constraints on the Skaergaard Liquid Line of Descent. *Lithos* **2006**, *92*, 154–180. https://doi.org/10.1016/j.lithos.2006.03.031.
69. Botcharnikov, R.E.; Koepke, J.; Holtz, F.; McCammon, C.; Wilke, M. The Effect of Water Activity on the Oxidation and Structural State of Fe in a Ferro-Basaltic Melt. *Geochimica et Cosmochimica Acta* **2005**, *69*, 5071–5085. https://doi.org/10.1016/j.gca.2005.04.023.
70. Husen, A.; Almeev, R.R.; Holtz, F. The Effect of H2O and Pressure on Multiple Saturation and Liquid Lines of Descent in Basalt from the Shatsky Rise. *Journal of Petrology* **2016**, *57*, 309–344. https://doi.org/10.1093/petrology/egw008.
71. Hossein-Zadeh, S. Estimation of Moho Depth in Iran by Combination of Gravity and Seismic Data, Institude for advanced studies in basic sceineces, Gava Zang: Znajan, Iran, 2012.
72. Sepahvand, M.R. Variations of Moho Depth and Vp/Vs Ratio in Central and Eastern Iran Using the Zhu and Kanamori Method, Kerman Graduate University of Technology (KGUT): Kerman, Iran, 2016.
73. LeBas, M.J. The Role of Aluminium in Igneous Clinopyroxenes with Relation to Their Parentage. *Am. J. Sci.* **1962**, *260*, 267–288.
74. Kilinc, A.; Carmichael, I.S.E.; Rivers, M.L.; Sack, R.O. The Ferric-Ferrous Ratio of Natural Silicate Liquids Equilibrated in Air. *Contr. Mineral. and Petrol.* **1983**, *83*, 136–140. https://doi.org/10.1007/BF00373086.
75. Kress, V.C.; Carmichael, I.S.E. The Compressibility of Silicate Liquids Containing Fe2O3 and the Effect of Composition, Temperature, Oxygen Fugacity and Pressure on Their Redox States. *Contr. Mineral. and Petrol.* **1991**, *108*, 82–92. https://doi.org/10.1007/BF00307328.
76. Moretti, R. Polymerisation, Basicity, Oxidation State and Their Role in Ionic Modelling of Silicate Melts. *Annals of Geophysics* **2005**, *48*. https://doi.org/10.4401/ag-3221.
77. Ottonello, G.; Moretti, R.; Marini, L.; Vetuschi Zuccolini, M. Oxidation State of Iron in Silicate Glasses and Melts: A Thermochemical Model. *Chemical Geology* **2001**, *174*, 157–179. https://doi.org/10.1016/S0009-2541(00)00314-4.
78. France, L.; Ildefonse, B.; Koepke, J.; Bech, F. A New Method to Estimate the Oxidation State of Basaltic Series from Microprobe Analyses. *Journal of Volcanology and Geothermal Research* **2010**, *189*, 340–346. https://doi.org/10.1016/j.jvolgeores.2009.11.023.
79. Chinner, G.A. Pelitic Gneisses with Varying Ferrous/Ferric Ratios from Glen Clova, Angus, Scotland. *Journal of Petrology* **1960**, *1*, 178–217.
80. Rumble, D. Fe-Ti Oxide Minerals from Regionally Metamorphosed Quartzites of Western New Hampshire. *Contr. Mineral. and Petrol.* **1973**, *42*, 181–195. https://doi.org/10.1007/BF00371584.
81. Powell, R.; Sandiford, M. Sapphirine and Spinel Phase Relationships in the System FeO-MgO-Al2O3-SiO2-TiO2-O2 in the Presence of Quartz and Hypersthene. *Contr. Mineral. and Petrol.* **1988**, *98*, 64–71. https://doi.org/10.1007/BF00371910.
82. Clarke, G.L.; Powell, R.; Guiraud, M. Low-Pressure Granulite Facies Metapelitic Assemblages and Corona Textures from MacRobertson Land, East Antarctica: The Importance of Fe203and TiOz in Accounting for Spinel-Bearing Assemblages. *Journal of Metamorphic Geology* **1989**, *7*, 323–335. https://doi.org/10.1111/j.1525-1314.1989.tb00600.x.
83. Ague, J.J.; Baxter, E.F.; Eckert, J.O., JR High fO2 During Sillimanite Zone Metamorphism of Part of the Barrovian Type Locality, Glen Clova, Scotland. *Journal of Petrology* **2001**, *42*, 1301–1320. https://doi.org/10.1093/petrology/42.7.1301.
84. Evans, K.A. Redox Decoupling and Redox Budgets: Conceptual Tools for the Study of Earth Systems. *Geology* **2006**, *34*, 489–492. https://doi.org/10.1130/G22390.1.
85. Diener, J.F.A.; Powell, R. Influence of Ferric Iron on the Stability of Mineral Assemblages. *Journal of Metamorphic Geology* **2010**, *28*, 599–613. https://doi.org/10.1111/j.1525-1314.2010.00880.x.

 doi:10.20944/preprints202504.0525.v2

86. Eugster, H.P. Reduction and Oxidation in Metamorphism. *Researches in Geochemistry (ed. Ableson, P.H.)* **1959**, 397–426.
87. Huebner, J.S. Buffering Techniques for Hydrostatic Systems at Elevated Pressures. In *Research Techniques for High Pressure and High Temperature*; Ulmer, G.C., Ed.; Springer: Berlin, Heidelberg, 1971; pp. 123–177 ISBN 978-3-642-88097-1.
88. Spear, F.S. *Metamorphic Phase Equilibria and Pressure–Temperature–Time Paths*; Mineralogical Society of America: Washington DC, 1993; ISBN 939950 34 0.
89. Aoki, K.-I.; Shiba, I. Pyroxenes from Lherzolite Inclusions of Itinome-Gata, Japan. *Lithos* **1973**, *6*, 41–51. https://doi.org/10.1016/0024-4937(73)90078-9.